6246–6263 *Nucleic Acids Research, 2023, Vol. 51, No. 12* *Published online 5 May 2023*
https://doi.org/10.1093/nar/gkad363

Replisome dysfunction upon inducible TIMELESS degradation synergizes with ATR inhibition to trigger replication catastrophe

Jinal A. Patel[1], Camryn Zezelic[1], Julie Rageul[1], Joanne Saldanha[2], Arafat Khan[1] and Hyungjin Kim[1,3,*]

[1]Department of Pharmacological Sciences, State University of New York at Stony Brook, Stony Brook, NY 11794, USA, [2]The Graduate program in Genetics, State University of New York at Stony Brook, Stony Brook, NY 11794, USA and [3]Stony Brook Cancer Center, Renaissance School of Medicine at Stony Brook University, Stony Brook, NY 11794, USA

Received January 03, 2023; Revised March 29, 2023; Editorial Decision April 21, 2023; Accepted April 26, 2023

ABSTRACT

The structure of DNA replication forks is preserved by TIMELESS (TIM) in the fork protection complex (FPC) to support seamless fork progression. While the scaffolding role of the FPC to couple the replisome activity is much appreciated, the detailed mechanism whereby inherent replication fork damage is sensed and counteracted during DNA replication remains largely elusive. Here, we implemented an auxin-based degron system that rapidly triggers inducible proteolysis of TIM as a source of endogenous DNA replication stress and replisome dysfunction to dissect the signaling events that unfold at stalled forks. We demonstrate that acute TIM degradation activates the ATR-CHK1 checkpoint, whose inhibition culminates in replication catastrophe by single-stranded DNA accumulation and RPA exhaustion. Mechanistically, unrestrained replisome uncoupling, excessive origin firing, and aberrant reversed fork processing account for the synergistic fork instability. Simultaneous TIM loss and ATR inactivation triggers DNA-PK-dependent CHK1 activation, which is unexpectedly necessary for promoting fork breakage by MRE11 and catastrophic cell death. We propose that acute replisome dysfunction results in a hyper-dependency on ATR to activate local and global fork stabilization mechanisms to counteract irreversible fork collapse. Our study identifies TIM as a point of replication vulnerability in cancer that can be exploited with ATR inhibitors.

GRAPHICAL ABSTRACT

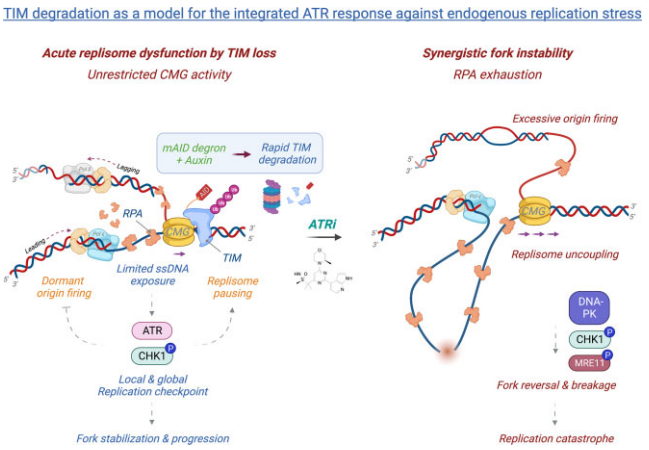

INTRODUCTION

Protecting DNA replication forks from a variety of intrinsic and extrinsic genotoxic stress is fundamental in maintaining genomic integrity and suppressing tumorigenesis (1). Improper control over DNA replication stress results in disruption of replisome activity and fork stalling, leading to replication gaps, lethal strand breakage, and fork collapse (2,3). The ATR (ataxia telangiectasia-mutated and rad3-related) kinase is a pivotal regulator of replication stress signaling to coordinate the cell cycle, DNA replication and DNA repair (4). ATR is stimulated by its two known activators, TOPBP1 and ETAA1 at stalled forks, and recruited to RPA-coated single-stranded DNA (ssDNA) (5). ATR-mediated phosphorylation of its downstream targets, including CHK1, prevents collapse of stalled forks by controlling fork stabilization and remodeling, promoting dNTP production and enforcing the S-G2-M checkpoints (6–9).

*To whom correspondence should be addressed. Email: hyungjin.kim@stonybrook.edu

Besides its activity in the replication stress response, ATR plays key roles in ensuring the integrity of ongoing replication forks. While immediate stress near the active replicon triggers a compensatory firing of dormant origins, late dormant origins are largely suppressed by ATR to limit ssDNA exposure and prevent RPA depletion (10,11). A basal-level activity of ATR continuously monitors the levels of RPA at active forks (12). Conversely, genetic or pharmacological inactivation of ATR results in exhaustion of available RPA pools as ssDNA accumulates, ultimately leading to fork collapse and a pathological endpoint of replication stress called replication catastrophe (13,14). ATR activation suppresses the initiation of DNA replication at dormant origins through the local phosphorylation of MCMs and FANCI, whereas ATR inhibition unleashes origin firing through an increase in phosphorylation of the GINS complex within the replisome (15–17). Additionally, ATR-dependent CHK1 phosphorylation promotes degradation of CDC25A phosphatase and suppresses CDK activation, thereby limiting origin firing at late S phase and restricting mitotic entry (18,19). While the role of ATR for stabilizing stressed forks is largely appreciated, how ATR monitors the replisome activity and deploys distinct fork stabilization mechanisms to counteract inherent damage originating from endogenous replication stress remains elusive.

The structure of a replication fork is maintained by the fork protection complex (FPC), composed of the TIMELESS (TIM)-TIPIN heterodimer (Swi1–Swi3 in *S. pombe*, and Tof1–Csm3 in *S. cerevisiae*) together with CLASPIN and AND-1 (20). Additionally, SDE2, a PCNA-associated replication stress regulator, interacts with TIM to promote its localization and stability at active forks (21–24). The FPC is essential for tethering the CMG (CDC45, MCM2–7, GINS) helicase and polymerases movement to prevent their uncoupling, thereby preventing the accumulation of ssDNA at replication forks. *In vitro*, TIM-TIPIN accelerates leading-strand replication in a CLASPIN-dependent manner, and recent structural studies have revealed that TIM-TIPIN grips duplex DNA ahead of the CMG, allowing efficient strand separation and replisome progression (25–28). Positioning of TIM in front of the replisome also implicates its role in restricting the CMG activity. At stalled forks, TIM-TIPIN directly interact with RPA-ssDNA to recruit CLASPIN and facilitate ATR-dependent CHK1 phosphorylation (29–31). Additional multifaceted roles of TIM, including telomere replication, cohesion establishment, management of difficult-to-replicate regions, and inhibition of origin firing in response to DNA damage have been reported, highlighting the pivotal role of TIM in preserving replication fork integrity at both active and stalled forks (32). Furthermore, the FPC works as a replication-pausing complex at various fork barriers in the genome, presumably preventing replisome uncoupling until DNA damage is resolved (33). While Rad53 (CHK1) is implicated in coupling leading- and lagging-strand DNA synthesis under replication damage in a Mrc1 (CLASPIN)-Tof1-dependent manner (34), how the ATR checkpoint controls the FPC at stalled forks is poorly understood. Conversely, the regulatory mechanism through which the FPC controls the dynamic process of DNA replication in conjunction with ATR remains uncharacterized.

Much of the effort made to dissect ATR-dependent replication stress response has been carried out under the conditions of DNA damage inflicted by exogenous genotoxins and chemotherapy. Moreover, it is challenging to monitor the molecular events at replication forks via conventional loss-of-function approaches that target replication genes including TIM, as disrupting the replication process results in pleiotropic cell cycle defects and is lethal to cells during long-term depletion of a target gene. To overcome this limitation, we have implemented the use of an auxin-inducible degron (AID) system that acutely manipulates endogenous TIM levels as a means to trigger replisome dysfunction, thus enabling us to specifically monitor the events unfolding upon acute TIM degradation at ongoing forks without deregulating cell cycle (35). In this study, we establish an indispensable role of ATR, both locally and globally, in counteracting replication catastrophe against endogenous replication damage caused by replisome dysfunction as a result of acute TIM loss. Our work also identifies activation of DNA-PK and CHK1-dependent signaling that leads to synergistic fork instability upon the loss of two essential genome caretakers, TIM and ATR, and provides mechanistic insight into how replisome dysfunction is sensed to engage distinct replication stress signaling in both ATR-dependent and independent manners.

MATERIALS AND METHODS

Reagents and biological resources

Information on antibodies, chemicals, kits, cell lines and DNA/RNA oligonucleotides can be found on Supplementary Table S1.

Cell culture

U2OS and HEK293T cell lines were acquired from the American Tissue Culture Collection (ATCC), HCT116 OsTRI1 F74G cells were a gift from Dr Masato Kanemaki (National Institute of Genetics, Japan). Cells were cultured in Dulbecco's modified Eagle's medium (U2OS and HEK293T) or McCoy's 5A medium (HCT116 OsTIR1 F74G and HCT116 OsTIR1 F74G TIM-mAID) supplemented with 10% fetal bovine serum and 1% penicillin/streptomycin, following standard culture conditions and procedures.

Plasmids

pSpCas9(BB)02A-Puro (PX459) V2.0 was a gift from Dr Feng Zhang (Addgene plasmid #62988) and ligated with annealed oligos containing restriction sites and sgRNA target sequence to generate the PX459-sgRNA F73. pMK286 (mAID-NeoR) was a gift from Dr Masato Kanemaki (Addgene plasmid #72824). pAcGFP-C1-RPA123-P2A was a gift from Dr Claudia Lukas (13). Homology sequences to the C-terminal end of *TIM* was obtained through gene synthesis and ligated to pUC57 (Gene Universal), which was used to generate the pUC57-mAID-NeoR donor template using Gibson assembly. Four mutations in the target sequence were made during gene synthesis and an additional PAM site mutation was generated through site-directed mutagenesis (SDM). pcDNA3-Flag-MRE11 was

synthesized from Genscript (SC1200/M). Primers containing overlapping homology sequences or mutations were used for Gibson Assembly and SDM, respectively. The ligated products were transformed into DH5α competent cells, with the exception of the px459-sgRNA F73 which was transformed into NEB Stable (C3040H; New England BioLabs) competent cells. Individual colonies were inoculated in Luria-Bertani (LB) media for DNA extraction using DNA miniprep or midiprep kits (Promega). All mutations and plasmid sequences were verified by Sanger DNA sequencing (Stony Brook University Genomic Facility).

Generation of HCT116 OsTIR1 F74G TIM-mAID cell line via CRISPR/cas9 gene editing

HCT116 CMV-OsTIR1 F74G cells were plated for 70–90% confluency one day before transfection which was done using the X-tremeGENE HP DNA Transfection reagent (Millipore Sigma) according to the manufacturer's protocol. Briefly, Opti-MEM, 1 μg of pX459-based CRISPR/Cas9 plasmid (encoding sgRNA targeting the 3′ UTR region of *TIM* and SpCas9), 1 μg of the pUC57 donor plasmid encoding a mAID-Neo^R cassette and homology arms, and X-tremeGENE transfection reagent (2:1 ratio of reagent to DNA) were mixed and incubated for 15 min at RT in the dark. The mixture was applied to cells in a dropwise fashion and incubated at 37°C for 30 h. Cells were then trypsinized and plated into 10 cm dishes with media containing puromycin (2 μg/ml) and neomycin (Geneticin/G418 substrate) (400 μg/ml). Puromycin containing medium was removed after 24 h and cells were continuously treated with media containing only neomycin for another 48–72 h. Single cells were plated into 96-well plates and neomycin resistant clones were eventually sub-cultured into 6-well plates and collected for Western blotting to detect mini-AID (mAID) expression levels and genomic DNA PCR to detect homologous recombination.

DNA and siRNA transfection

Unless otherwise stated, plasmid transfection was performed using Lipofectamine LTX (Millipore Sigma) according to the manufacturer's protocols. siRNA duplexes were transfected at 20 nM (unless otherwise indicated) using Lipofectamine RNAiMAX (Thermo Fisher).

T7 endonuclease I assay

To determine sgRNA targeting efficiency, U2OS cells were transfected with 1 μg of pX459-based CRISPR/Cas9 plasmid (encoding sgRNA targeting the 3′ UTR region of *TIM* and SpCas9) for 48 h. Cells were then selected with puromycin for an additional 48–72 h. Transfected cells were trypsinized, washed once with ice-cold PBS, resuspended in 200 μl of RT PBS and added to a tube containing 20 μl of proteinase K (Qiagen). Genomic DNA was extracted using a QiaAMP DNA mini kit (Qiagen) according to the manufacturer's protocol. To determine the sgRNA targeting efficiency, the EnGen detection mutation kit (New England BioLabs) was used according to the manufacturer's protocol. Briefly, primers (5′ EnGen gDNA TIM forward and 3′ EnGen gDNA TIM reverse) were designed to amplify a 854 bp region containing the target site, which was offset from the center of the amplicon to generate two fragments of 500 and 313 bp. A PCR reaction containing 200 ng of genomic DNA, 0.5 μM of each primer, and 1X of the Q5 hot start high-fidelity 2X master mix was set up to amplify the target region. Following the PCR reaction, 1 μl was checked on an agarose gel to verify amplification of the 854 bp fragment. Heteroduplex formation was completed by assembling an annealing reaction containing 5 μl of the PCR reaction in 10X NEB buffer 2 and nuclease-free water and incubated in a water bath at 95°C for 10 min and allowed to cool to RT (overnight). 1 μl of T7 endonuclease 1 (T7E1) was added to the sample and incubated at 37 °C for 15 min to promote digestion of mismatched duplexes, followed by incubation with 1 μl of proteinase K at 37°C for 5 min to inactivate T7E1 enzymatic activity. Undigested and digested samples were run on an agarose gel for fragment analysis.

Genomic DNA extraction and PCR

To detect homologous recombination in neomycin resistant clones, cells were grown in a six-well plate and collected for genomic DNA extraction and subjected to PCR analysis with specific primers. Resistant clones were trypsinized and washed once with PBS and resuspended in a RT PBS for DNA extraction using a QiaAMP DNA mini kit (Qiagen) according to the manufacturer's protocol, as mentioned previously.

Drug treatments

5-Phenyl-1H-indole-3-acetic acid (5-Ph-IAA) dissolved in DMSO to 10 and 1 mM stocks, treated at 1 μM; AZD6738 (ATRi) dissolved in DMSO to 10 and 1 mM stocks, treated at 1 μM; NU7441 (DNA-PKi) dissolved in DMSO at 5 mM stocks, treated at 5 μM; MK8776 (CHK1i) dissolved in DMSO to 10 mM stock, treated at 5 μM; KU55933 (ATMi) dissolved in DMSO at 10 mM stocks, treated at 10 μM; SNS-032 (CDK2i) dissolved in DMSO to 10 mM stock, treated at 5 μM; PHA-767191 (CDC7i) dissolved in DMSO to 10 mM stock, treated at 5 μM; Aphidicolin (APH) (Millipor Sigma) was dissolved in DMSO at 30 mM stock, treated at 1 μM; in cell culture media for the indicated times. Hydroxyurea (HU) (Millipore Sigma) was dissolved in water at 500 mM stock and diluted to either 2 mM for 4 h (Western blotting) or 500 μM (γH2AX flow cytometry experiments) in cell culture media that was equilibrated overnight in the incubator. Camptothecin (CPT) (Millipore Sigma) was dissolved in DMSO and used at 1 μM in cell culture media for indicated experiments and times.

Cell synchronization

Cells were synchronized at the G1/S boundary using a double thymidine block protocol. Thymidine (Millipore Sigma) was dissolved in PBS at 100 mM stock and treated at 2 mM. Briefly, cells were seeded at 30% confluency, allowed to attached for 24 h and then treated with 2 mM of thymidine in cell culture media for 17 h (first dose). Cells were washed three times with warm PBS and replenished with

fresh thymidine-free medium for 9 h. Finally, cells were then treated with 2 mM thymidine for an additional 17 h (second dose) before being released into fresh medium as indicated.

Cell lysis, fractionation, and western blotting

Cells were collected by trypsinization, washed in ice-cold phosphate-buffered saline (PBS) and lysed in lysis buffer complemented with cOmplete™, EDTA-free protease inhibitor cocktails (Roche) and Halt™ phosphatase inhibitor cocktails (Thermo Fisher) for 40 min on ice. NETN300 (50 mM Tris–HCl pH 7.5, 300 mM NaCl, 0.2 mM EDTA, 1% NP40) was used for whole-cell lysis. The lysates were then cleared by centrifugation at 15 000 rpm at 4 °C for 10 min. For subcellular fractionation, cells were lysed using lysis (S) buffer (10 mM HEPES pH 7.4, 10 mM KCl, 0.05% NP-40) for 15 min on ice. After centrifugation at 14 000 rpm for 10 minutes, pellets were washed with lysis (S) buffer and then resuspended in PBS. Equal amount of 2X boiling lysis buffer (50 mM Tris–HCl pH 6.8, 2% SDS, 850 mM β-mercaptoethanol) and incubated at 95°C for 10–15 min with occasional vortexing. For chromatin extraction, cells were lysed used lysis (S) buffer for 15 min on ice and cleared by centrifugation at 14 000 rpm for 10 min (supernatant containing cytosolic proteins was saved as the S fraction). The pellet (nuclei) was washed with lysis (S) buffer, resuspended in P1 low salt buffer (10 mM Tris–HCl pH 7.5, 0.2 mM $MgCl_2$, 1% Triton X-100) and incubated on ice for 15 min and centrifuged (supernatant containing nuclear and nonchromatin-associated proteins was saved as the P1 fraction). The pellet (chromatin) was washed with P1 low salt buffer, resuspended in 0.2 N HCl and incubated on ice for 20 min. After centrifugation, supernatant was transferred into a tube containing an equal volume of Tris–HCl (pH 8.0) to neutralize acid (these acid-soluble chromatin-associated proteins were saved as the P2 fraction). The protein concentration of supernatants was measured using the Bradford assay (Bio-Rad) so that 25–50 μg of protein was loaded onto an SDS-PAGE gel and transferred to PVDF membranes (Millipore Sigma). Membranes were incubated with the indicated primary and horseradish peroxidase (HRP)-conjugated secondary antibodies, and HRP signals were detected by enhanced chemiluminescence (ECL) Western blotting substrates (Thermo Fisher) using the iBright digital imager (CL1000; Thermo Fisher). Antibody information can be found in Key Resources Table.

RT-qPCR

RNA was isolated using TRIzol (Invitrogen) and chloroform (Millipore Sigma). cDNA synthesis was performed using a high-capacity cDNA reverse transcription kit (Applied Biosystems) according to the manufacturer's protocol. Real-time quantitative PCR was performed using Fast SYBR Green Master Mix (Applied Biosystems) and a QuantStudio3 Real Time PCR system (Thermo Fisher). *GAPDH* mRNA levels were used as a control for normalization. The following primers were used for cDNA amplification: *ETAA1* forward 5′-TCCTTGTACTCCCAGTGTAG-3′; *ETAA1* reverse 5′-TTGAATCACATCTAGCTCTTCC-3′.

DNA fiber analysis

Exponentially growing or synchronized cells were first treated for the indicated times and then pulse-labeled with 50 μM 5-chloro-2′-deoxyuridine (CldU) for 30 min, washed three times with PBS, then pulse-labeled with 250 μM 5-iodo-2′-deoxyuridine (IdU) for 30 min prior to harvesting. All necessary media was equilibrated overnight at 37°C under 5% CO_2. Cells were harvested by trypsinization and washed with PBS. DNA fibers were then prepared by spreading. In brief, cells were resuspended to 1×10^6 cells/ml in ice-cold PBS and 2000–4000 cells were spotted on a glass slide. Fiber lysis solution (50 mM EDTA, 0.5% SDS, 200 mM Tris–HCl pH7.5) was added on top of the drop and gently stirred with the pipette tip and incubated for 5 min. Slides were carefully tilted 15° to allow fibers to spread along the slide and then placed horizontally to air dry for 10–15 min (in the dark). DNA was fixed by immersing the slides in freshly prepared methanol/acetic acid solution (3:1) for 5 min at RT in the dark. Slides were allowed to dry and then washed twice in PBS for 5 min at RT. DNA was denatured in a 2.5 mM HCl solution for one hour at RT in the dark. Slides were washed three times in PBS for 5 min and placed horizontally, all subsequent immunostaining incubations were performed in dark and humidified conditions at RT. In short, slides were blocked with 5% BSA for 30–45 min, then two primary antibodies were diluted in 1% BSA in PBS-Tween 0.5% (PBS-T) (rat monoclonal anti-BrdU for CldU, 1:200, and mouse monoclonal anti-BrdU for IdU, 1:20) and incubated for 2 h. After washed slides three times in PBS-T for 5 min, two secondary antibodies were diluted in 1% BSA in PBS-T (Alexa Fluor 594 goat anti-rat and Alexa Fluor 488 goat anti-mouse, 1:400) and incubated for one hour. Slides were washed three times in PBS-T for 5 min and allowed to dry completely. Coverslips were applied on top of the slides with ProLong™ Gold Antifade and allowed to cure overnight at RT. DNA fibers were then imaged with the Eclipse Ts2R-FL inverted fluorescence microscope (Nikon) equipped with the Nikon DSQi2 digital camera, or LSM880 microscope (Carl Zeiss), and analyzed using Fiji and Prism (GraphPad).

Flow cytometry

For cell cycle analysis, cells were treated as indicated and collected by trypsinization, and washed once with PBS. Cells were then washed once with 1% BSA in PBS, vortexed briefly and centrifuged at 500*g* for 5 min at RT. Cells were resuspended and homogenized in a small volume of 1X PBS, before being fixed with 70% ethanol, which was added dropwise while vortexing at a low speed. Fixed cells were kept at 4°C for at least 1 h to overnight before being processed. After fixation, ethanol was removed via centrifugation at 500*g* for 5 min at 4 °C and cells were washed twice with PBS. Finally, cells were resuspended in PBS containing 200 μg/ml PureLink™ RNase A and eBioscience™ 7-AAD viability staining solution (Thermo Fisher) and incubated for 30 min at 37°C. For EdU staining, treated cells were incubated with 10 μM 5-Ethynyl-2′-Deoxyuridine (EdU) (Thermo Fisher) for 30 min prior to harvest, to label replicating cells. Harvested cells were fixed with 70% ethanol for at least 1 h to overnight at 4°C before being processed. Cells

were subjected to EdU-click reaction using Alexa Fluor 488 picolyl azide and click-iT plus EdU flow cytometry assay kit (Thermo Fisher) following the manufacturer's protocol. Cells were washed once and resuspended in PBS containing 200 μg/ml PureLink™ RNase A and eBioscience™ 7-AAD viability staining solution (Thermo Fisher) and incubated for 30 min at 37 °C. For detecting γH2AX, treated cells were processed using the Foxp3/transcription factor staining buffer set (Thermo Fisher) according to the manufacturer's protocol. Briefly, harvested cells were washed once with PBS, permeabilized using 0.5% Triton-X in PBS for 10 min at 4°C, washed with 1% BSA in PBS. Following centrifugation at 400*g* for 5 min, cells were fixed in Foxp3 fixation/permeabilization solution for one hour at room temperature (RT). Cells were then washed with 1X permeabilization buffer, centrifuged at 400*g* for 5 min and incubated with Alexa Fluor 488-conjugated γH2AX (1:100; CR55T33, Thermo Fisher) in Foxp3/transcription factor staining buffer (Thermo Fisher) for 1 h at RT in the dark. Cells were washed once and resuspended in PBS containing 200 μg/ml PureLink™ RNase A and eBioscience™ 7-AAD viability staining solution (Thermo Fisher) and incubated for 30 min at 37°C (for indicated experiments) or else were resuspended in PBS. For chromatin-bound RPA32 detection, treated cells were processed as mentioned above and incubated with mouse anti-RPA32 (1:100, NA19, Millipore Sigma) for one hour at RT in the dark. Cells were washed once and incubated with Alexa Fluor 488 goat anti-mouse secondary antibody (1:1000, A11029, Life Technologies) for 30 min at RT in the dark. Cells were washed once and resuspended in PBS. For BrdU staining, cells were treated with 10 μM 5-bromo-2′-deoxyuridine (BrdU) for 24 h to label nascent DNA, washed three times with PBS followed by 5-Ph-IAA and/or ATRi (AZD6738) treatment at 1 μM for 8 h. Harvested cells were processed as mentioned above and incubated with mouse anti-BrdU (1:100, MA3-071, Thermo Fisher) for one hour at RT in the dark. Cells were washed once and incubated with Alexa Fluor 488 goat anti-mouse secondary antibody (1:1000, A11029, Thermo Fisher) for 30 min at RT in the dark. Cells were washed once and resuspended in PBS. All samples were analyzed with the Attune NxT acoustic focusing cytometry (Thermo Fisher) and analyzed with the Attune NxT software v2.7 (Thermo Fisher).

Cell proliferation assay

150 000 cells were seeded into 35 mm dishes and left untreated or were treated with 1 μM 5-Ph-IAA continuously for five days. Cells were counted every 24 h for four days and cellular proliferation were measured with trypan blue staining using a Countess 3 automated cell counter. Proliferation was expressed as fold change (ratio over day 0).

Cell survival and colony formation assays

For cell survival, cells were seeded into 96-well plates and treated with 1 μM 5-Ph-IAA and/or inhibitors (as indicated) continuously for 72 h or for 24 h and replenished with drug-free media. Cell viability was determined using the CellTiter-Glo luminescent cell viability assay (Promega). Luminescence was measured using a GloMax Explorer microplate luminometer (Promega). For colony formation, cells were seeded at 1000 cells/well in six-well plates and treated with 5-Ph-IAA and/or inhibitors (as indicated) for 24 h and replenished with drug-free media (changed every 3–4 days) and monitored for ten days. Cells were washed once with PBS and fixed with ice-cold methanol for 10 min at −20°C. Cells were then stained with 0.5% w/v crystal violet staining solution (C581-25, Thermo Fisher) for 10 min at RT. Staining solution was retrieved, plates were carefully rinsed in water and allowed to dry at RT. Colonies were counted manually.

Proximity ligation assay (PLA) on nascent DNA

Cells were grown on poly-L-lysine coated glass coverslips and treated for 8h with the indicated drugs. Twelve minutes before the end of treatment, EdU was added to the media at a final concentration of 125 μM. Cells were fixed with 4% PFA for 10 min at RT, washed in PBS and stored overnight at 4 °C in fresh PBS and wrapped in foil. Cells were then permeabilized with 0.3% Triton X-100 in PBS for 3 min on ice. Following PBS washes, a Click-iT reaction was performed to tag the EdU alkyne using 10 μM biotin-azide, 2 mM $CuSO_4$ and 10 mM sodium ascorbate for 1 h at RT in a humidified chamber protected from light. Cells were then washed in PBS once before proceeding with the PLA assay between biotin-labeled nascent DNA and MCM6 following the manufacturer's instructions (Duolink, Millipore Sigma). Rabbit anti-biotin antibody (Bethyl Laboratories, #A150-109A; 1:3000) was used together with either mouse anti-MCM6 (Santa Cruz, sc-393618, 1:500) or mouse anti-biotin (Jackson ImmunoResearch, #200-002-211, 1:2000) to control for EdU uptake. Coverslips were mounted on slides and imaged with an Eclipse Ts2R-FL inverted Nikon fluorescence microscope equipped with a Nikon DSQi2 camera. Images were analyzed using the NIS-Elements Research BR software (Nikon) and quantifications were analyzed using Prism (GraphPad).

Immunofluorescence

Coverslips were coated with poly-L-lysine (Millipore Sigma) for 15 min, and cells were seeded at least 24 h before any drug treatments. Following treatments, cells were washed once with cold PBS on ice and fixed with 4% paraformaldehyde for 10 min at RT. After three washes with PBS, cells were permeabilized with 0.3% Triton X-100 in PBS for 3 min on ice. Following permeabilization, cells were washed three times with cold PBS and blocked for 1 h at RT using 5% BSA in PBS. Subsequently, cells were incubated with primary antibodies diluted in 1% BSA for 2 h at RT. After three PBS washes, cells were incubated with secondary antibodies coupled to fluorophores diluted in 1% BSA for 45 min at RT. Following three additional washes with PBS, coverslips were mounted onto glass microscope slides using Vectashield mounting medium containing DAPI (Vector Lab). Coverslips were imaged with an Eclipse Ts2R-FL inverted fluorescence microscope (Nikon) equipped with a Nikon DSQi2 digital camera and analyzed using NIS-Elements, Research BR software (Nikon). Quantification data was processed using Prism (GraphPad).

DNA comet assay

DNA comet assay was performed using the CometAssay kit (4250-050-K, Trevigen) according to the manufacturer's protocol. Briefly, 25 μl of the sample cell suspension at 2×10^5 cells/ml were combined with 225 μl of low-melting agarose (LMAgarose) (1:10 ratio, v/v) and 50 μl of this mixture was quickly spread onto the provided comet slides (Trevigen). Following solidification at 4°C, slides were immersed in cold lysis solution for 1 h at 4°C then placed in freshly prepared alkaline unwinding solution (20 mM NaOH, 1 mM EDTA) for 20 min at RT. Electrophoresis of unwound DNA was performed at 21 V for 30 min. Slides were then washed twice with dH_2O for 5 min, dehydrated with 70% ethanol for 5 min, dried, and stained with SYBR Gold staining solution (Thermo Fisher) for 30 min. Comets were imaged at 10x magnification with an Eclipse Ts2R-FL inverted fluorescence microscope (Nikon) equipped with a Nikon DSQi2 digital camera and analyzed using OpenComet on Fiji and Prism (GraphPad). Up to at least 100 individual nuclei were evaluated per group.

Statistical analyses

Student's *t*-test was used to assess the statistical significance, using Prism (GraphPad). Unpaired *t*-tests were performed with a 95% confidence interval, using two-tailed *P*-values, unless stated otherwise. For the DNA fiber assay, distribution of track length or ratio were tested using a two-side Mann–Whitney *U*-test, with a 95% confidence interval, using Prism (GraphPad). Where indicated, Student's *t*-test was used to compare medians of replicates. Western blotting, survival and clonogenic assays and cell cycle analysis/flow cytometry experiments were representative of at least two, mostly three, biologically independent experiments and showed reproducible results.

RESULTS

The TIM-mAID system rapidly degrades endogenous TIM upon 5-ph-IAA treatment

To model replisome dysfunction at ongoing forks as a source of endogenous replication stress, we employed an AID technology, in which an F-box protein OsTIR1 stably expressed in HCT116 cells (Supplementary Figure S1A) integrates into the endogenous Skp1-Cullin-F-box (SCF) ubiquitin E3 ligase complex and recognizes the AID degron in an auxin-dependent manner, thus leading to the rapid degradation of degron-tagged endogenous TIM (Figure 1A). We used an upgraded bump-and-hole AID2 system, which employs the OsTIR F74G and auxin derivative 5-Ph-IAA pair to achieve enhanced degradation and avoid leaky degradation (36). To obtain homozygous alleles of degron-tagged *TIM*, we devised a CRISPR knock-in strategy to target an sgRNA guide to the *TIM* 3′ UTR region (verified by a T7E1 nuclease assay; Supplementary Figure S1B) in the presence of Cas9 and a homology donor plasmid that contains a mini-AID (mAID)-Neo^R cassette (Supplementary Figure S1C), thereby tagging a 68 amino acid fragment of AID onto the C-terminus of endogenous TIM (Figure 1B). Several clones expressing the mAID-tagged TIM were selected (Supplementary Figure S1D), and insertion of the mAID-Neo^R cassette was verified by genomic PCR (Figure S1E). Upon 5-Ph-IAA administration, three independent clones exhibited rapid depletion of mAID-TIM (Figure 1C), which was extremely efficient, exhibiting <30 min of half-life (Figure 1D). 5-Ph-IAA treatment also caused rapid downregulation of TIPIN, the obligate heterodimer of TIM that is required for the stability of TIM and vice versa, indicating that the overall integrity of the FPC is compromised (Figure 1D, E). Cellular mAID-TIM levels were restored once 5-Ph-IAA was removed, indicating that the AID system works in a reversible fashion (Figure 1F). Together, we have successfully established an AID degron system that achieves sharp proteolytic control of TIM, allowing us to scrutinize the events that unfold at the replication fork upon acute depletion of TIM and subsequent replisome dysfunction.

TIM-depleted cells exhibit replication defects but manage to progress through S phase

Our previous study demonstrated that siRNA-mediated TIM knockdown results in impaired fork progression, frequent fork stalling, and a defect in checkpoint activation upon exogenous replication stress (23). 5-Ph-IAA treatment in two independent TIM-mAID clones, but not in parental HCT116 cells, significantly impaired cell proliferation (Figure 2A). DNA fiber analysis of ongoing forks exhibited a significant shortening of DNA replication tracks in a 5-Ph-IAA-dependent manner, indicating that replication fork progression is compromised upon TIM degradation (Figure 2B and Supplementary Figure S2A). Additionally, defects in fork progression were observed as early as 4 h upon 5-Ph-IAA (Supplementary Figure S2B). TIM-mAID clones treated with 5-Ph-IAA also failed to induce CHK1 phosphorylation in response to hydroxyurea (HU), confirming that TIM is required for ATR-dependent CHK1 activation under replication damage (Figure 2C, D). Under HU damage, TIM depletion was associated with high levels of RPA32 phosphorylation at S4/S8, a marker for resection of DNA repair intermediates and strand breaks, representing an increase of unresolved replication stress (Figure 2C, D). Furthermore, γH2AX, a marker for DNA double strand breaks (DSBs), was evident upon 5-Ph-IAA treatment even in the absence of damage, which was much more elevated after HU treatment (Figure 2D, E). In order to illustrate the effect of TIM loss specifically in DNA replication, we synchronized cells at the G1/S boundary via double thymidine block and acutely depleted TIM by 5-Ph-IAA right before releasing cells into S phase. In control cells not exposed to 5-Ph-IAA, cells generally completed replication and started to come back to G1 within 6 h, followed by the second S phase of the cell cycle in 15 h post release (Figure 2F). Intriguingly, TIM-depleted cells exhibited only a mild delay in the first S phase progression, while its defect became more pronounced in the second S phase, due to a G2/M arrest and impaired G1/S progression (Figure 2F; 4 h versus 15 h). Supporting this, in the first S phase, we observed only a mild increase in DNA damage markers, including pKAP1

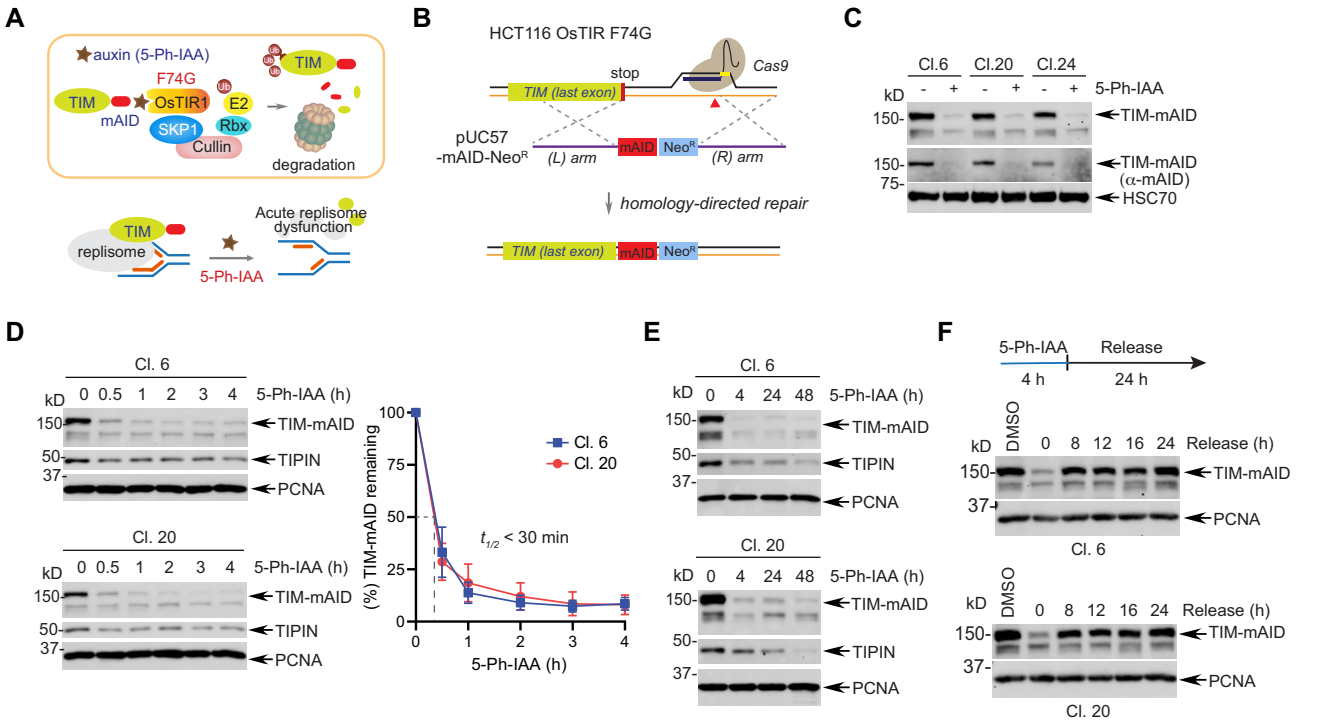

Figure 1. Establishment of the TIM-mAID degron system. **(A)** Schematic of auxin-inducible acute TIM-mAID degradation, leading to replisome disassembly. The AID2 system (the OsTIR1 F74G:5-Ph-IAA pair) is used. **(B)** Schematic depicting knock-in of the mAID-Neo^R cassette into the C-terminus of TIM by CRISPR-Cas9. **(C)** Western Blotting (WB) showing the degradation of TIM-mAID by treatment of 1 μM 5-Ph-IAA for 4 h in indicated clones. **(D)** *Left*: time-dependent rapid degradation of TIM-mAID. *Right*: kinetics of TIM-mAID degradation. $n = 3$, mean ± SD. A dotted line denotes half-life of degradation. **(E)** Degradation of TIM-mAID and TIPIN upon 5-Ph-IAA treatment. **(F)** Reversal kinetics of TIM-mAID following 5-Ph-IAA removal.

at S824 and pRPA32 at S4/S8 (Supplementary Figure S2C). In contrast, these signals were much more elevated in the second S phase when cells were exposed to 5-Ph-IAA (Figure 2G; 3 h versus 18 h). Together, these results suggest that accumulation of unresolved DNA damage caused by TIM depletion in the first S phase persists and is carried over into the next cell cycle, affecting the second round of DNA replication. Importantly, this suggests the existence of a mechanism that mitigates the replication damage caused by acute replisome dysfunction and allows cells to complete DNA replication.

ATR inhibition in the absence of TIM synergistically triggers replication damage

We sought to identify the mechanism operating at the replication fork responsible for alleviating the replication stress originating from acute replisome dysfunction and reasoned that the replication checkpoint kinase ATR is an ideal candidate. We treated an asynchronized population of HCT116 TIM-mAID cells with ceralasertib (AZD6738), an orally active and selective ATR inhibitor (ATRi) currently under phase I and II clinical trials, following acute TIM degradation (37). While cells exposed to 5-Ph-IAA or ATRi alone showed little signs of replication damage, combination of 5-Ph-IAA and ATRi dramatically intensified the levels of pRPA32 S4/S8 and pKAP1 S824 (Figure 3A; lanes 3 versus 6, B; lanes 2, 4, 6, 8, and Supplementary Figure S3A for quantification). Another independent clone showed a similar induction of replication damage only in the combination of 5-Ph-IAA and ATRi (Supplementary Figure S3B). Pre-treatment of ATRi before 5-Ph-IAA resulted in a similar synergistic induction of replication damage markers (Figure 3C; lanes 4 versus 7). The levels of synergistic increase in pRPA32 S4/S8 was comparable to siRNA TIM and ATRi combination (Supplementary Figure S3C). Additionally, immunofluorescence showed a dramatic increase in γH2AX signals, mostly exhibiting widespread pan-nuclear staining that represents lethal replication stress (38), in cells treated with 5-Ph-IAA and ATRi (Figure 3D, E). Furthermore, pre-exposure to 5-Ph-IAA for 4 h greatly enhanced the levels of pRPA32 S4/S8 compared to co-treatment of 5-Ph-IAA and ATRi for 4 h, reaching a similar level as continuous treatment for 8 h, indicating that acute TIM degradation sensitizes replication forks to ATR inhibition (Supplementary Figure S3D). In all the cases, we observed an elevation in pCHK1 S345 levels, indicating that an ATR-independent signaling mediates CHK1 activation during the synergistic replication damage caused by TIM and ATR deficiency. Phoshphorylation of RPA32 at S4/S8 was enriched at the chromatin-bound fraction in both asynchronous and G1/S synchronized cells, supporting the idea that replication damage originates at ongoing replication forks (Supplementary Figure S3E, F). The synergistic intensification of pKAP1 and pRPA32 signals was reversible upon removal of 5-Ph-IAA and ATRi, while

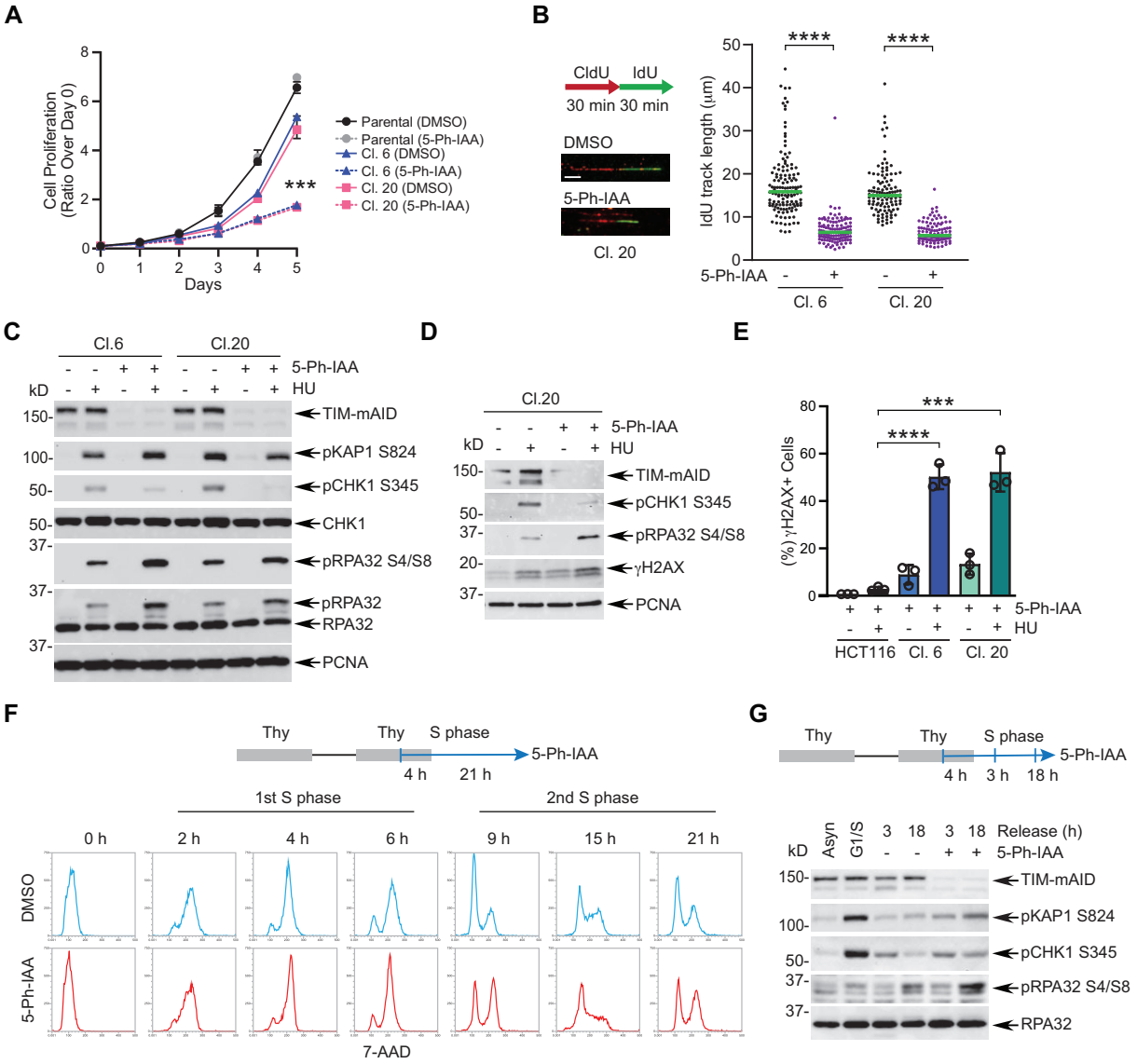

Figure 2. Effects of TIM-mAID degradation in DNA replication and S phase progression. (**A**) Cell proliferation of HCT116 OsTIR1 F74G parental versus TIM-mAID two independent clones upon 1 μM 5-Ph-IAA treatment. $n = 3 \pm$ SD, $^{***}P < 0.001$, two-way ANOVA. (**B**) Dot plot and median of the IdU track length upon 5-Ph-IAA treatment for 48 h. Representative DNA fibers are shown. Scale bar: 5 μm. $n = 2$, >200 tracks per condition, $^{****}P < 0.0001$, Mann–Whitney test. (**C, D**) WB analysis of CHK1, RPA32 and H2AX phosphorylation following 5-Ph-IAA treatment for 24 h and 2 mM HU in last 4 h. (**E**) Percentage of γH2AX-positive cells treated with 5-Ph-IAA for 24 h and 2 mM HU in last 4 h, then analyzed by flow cytometry. $n = 3$, mean ± SD, $^{****}P < 0.0001$, $^{***}P < 0.001$, Student's t-test. (**F**) Flow cytometry of TIM-mAID cells synchronized at G1/S by double thymidine block, depleted of TIM-mAID for 4 h by 5-Ph-IAA, and released into S phase. **(G)** HCT116 mAID-TIM cells were synchronized at G1/S, depleted of TIM by 1 μM 5-Ph-IAA for 4 h, and harvested at 3 h (first S phase) or 18 h (second S phase) post release to analyze replication damage markers by WB.

replication damage was irreparable, leading to increased cleavage of PARP1 (cPARP1), an indicator for apoptotic cell death (Figure 3F; lanes 5, 9, 13). Similarly, continuous exposure to 5-Ph-IAA and ATRi together led to an induction of replication-associated DSBs (γH2AX), PARP1 cleavage, and synergistic loss of viability as measured by cellular ATP assays (Figure 3G, H). Together, these results reveal that replication damage is synergistically accumulated in the absence of TIM and ATR, suggesting that acute TIM loss leads to a hyper-reliance on the ATR checkpoint to protect stalled forks.

Acute TIM degradation and ATR inhibition triggers catastrophic replication fork instability

By taking advantage of the AID system to rapidly control TIM levels without affecting cell cycle, we further sought to monitor the replication stress evident at stalled forks without TIM. To this end, we synchronized TIM-mAID cells at the G1/S boundary, acutely depleted TIM, and let cells traverse through S phase in the presence or absence of ATRi. Remarkably, only the cells depleted of TIM and challenged with ATRi experienced a dramatic elevation of pRPA32 S4/S8 during S phase progression (i.e. 2–6 h post release) in

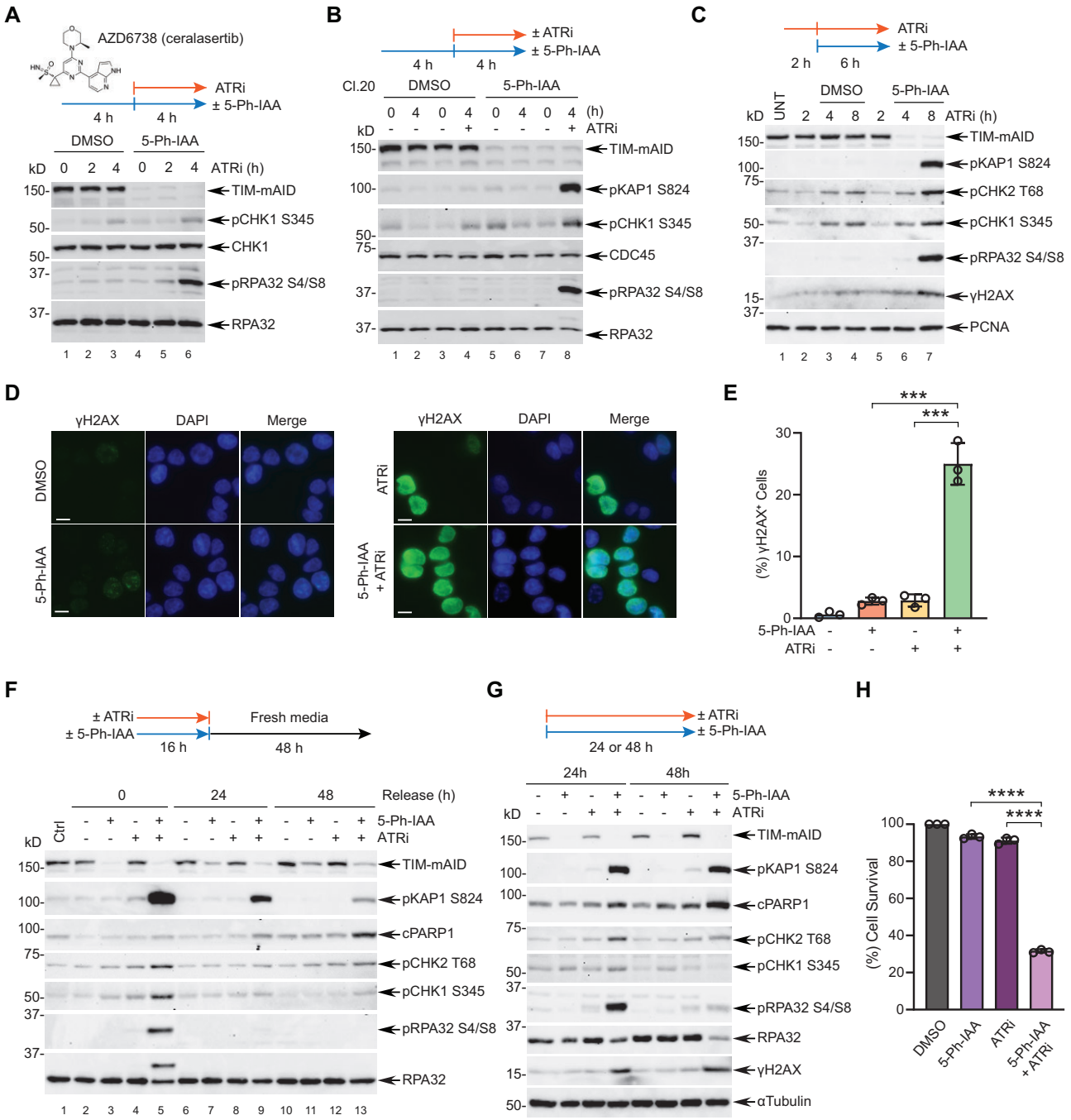

Figure 3. Acute TIM degradation and ATR inhibition synergistically triggers replication damage. (**A, B**) TIM-mAID cells (Cl.20) were treated with 1 μM 5-Ph-IAA and/or 1 μM AZD6738/ATRi (ceralasertib), and analyzed by WB. 0 h indicates 4 h pre-treatment of DMSO or 5-Ph-IAA. (**C**) TIM-mAID cells were pretreated with 1 μM ATRi followed by 5-Ph-IAA for the indicated times and analyzed by WB. (**D**) Representative images of γH2AX staining following treatment with 5-Ph-IAA and/or ATRi for 8 h in TIM-mAID cells. Scale bar, 10 μm. (**E**) Quantification of γH2AX-positive cells defined as >2200 mean fluorescence signals (arbitrary unit). $n = 3$, >500 nuclei per sample, $^{***}P < 0.001$, Student's t-test. (**F**) TIM-mAID cells were treated with 5-Ph-IAA and/or ATRi for 16 h and released into fresh media for 24 and 48 h, and cell death was evaluated by cleaved PARP1 (cPARP1) WB. (**G**) TIM-mAID cells were continuously treated with 5-Ph-IAA and/or ATRi for 24 or 48 h, and cell death analyzed by WB. (**H**) Cytotoxicity of TIM-mAID cells treated with 5-Ph-IAA and/or ATRi for 72 h, measured by ATP-dependent luminescence. $n = 3$, mean ± SD, $^{****}P < 0.0001$, Student's t-test.

contrast to 5-Ph-IAA or ATRi alone, suggesting that replisome dysfunction and ATR inhibition synergistically cause fork collapse (Figure 4A). Cells deficient in both TIM and ATR showed a synergistic decrease in their ability to incorporate EdU while in S phase, suggesting that combined TIM degradation and ATR inhibition impairs DNA synthesis (Figure 4B). Indeed, flow cytometric analysis revealed that cells exposed to both 5-Ph-IAA and ATRi have difficulty progressing through S phase (pronounced at 6 h after release) (Figure 4C). Accordingly, DNA replication tracks from cells in S phase were significantly shorter when both TIM and ATR are deficient (Figure 4D, E, and Supplementary Figure S4A). Moreover, a DNA comet assay directly demonstrated a synergistic elevation of DNA breaks in S-phase cells without TIM and ATR, further highlighting the essential role of ATR in suppressing fork collapse upon TIM loss during fork progression (Figure 4F, G). Together, these data reveal that when a replication fork is acutely impaired by the TIM loss, ATR becomes indispensable for DNA replication and cell cycle transition, and cells without both TIM and ATR are subject to a synergistic replication fork instability associated with fork collapse.

RPA exhaustion caused by replisome uncoupling and dormant origin firing underlies the synergistic fork instability upon TIM degradation and ATR inhibition

Next, we investigated the mechanism underlying the synergistic fork instability observed upon acute TIM degradation and ATR inhibition. Loss of TIM that normally supports the structure of the FPC causes uncoupling of the replisome, exposing stretches of ssDNA at stalled forks. In order to monitor cellular levels of ssDNA at stalled forks, we employed a flow cytometry-based method to quantify association of RPA to chromatin as a surrogate marker for ssDNA accumulation (39). Exposure of cells to 5-Ph-IAA or HU, which depletes dNTP pools and thus inhibits DNA synthesis, increased chromatin-bound RPA pools, and 5-Ph-IAA and HU in combination results in a further increase in RPA association to ssDNA in an additive manner, indicating that acute TIM depletion leads to ssDNA exposure (Supplementary Figure S4B). Remarkably, combined treatment of 5-Ph-IAA and ATRi, but not individual treatments, led to a dramatic accumulation of chromatin-bound RPA in a synergistic manner, evident from the appearance of a new RPA^+ peak, indicating that excessive ssDNA accumulates in the absence of both TIM and ATR (Figure 5A). The intensity of RPA foci from immunofluorescence also significantly increased in this condition (Supplementary Figure S4C) Similarly, much greater levels of BrdU-labeled parental-strand ssDNA were detected under non-denaturing conditions in cells exposed to 5-Ph-IAA and ATRi, in comparison to single treatment, representing synergistic ssDNA exposure at replication forks (Figure 5B). A series of recent studies suggest that RPA protects ssDNA at stalled forks and ssDNA accumulation over the RPA protection threshold results in RPA exhaustion and massive DNA breakage, thus leading to irreversible fork collapse also known as replication catastrophe (12,13,40). Consistent with this model, titration of RPA70, a subunit of the RPA complex, by siRNA-mediated knockdown exacerbated the effect of 5-Ph-IAA and ATRi, as revealed by the dramatic elevation of pRPA32 and pKAP1 as well as γH2AX with just 0.5 nM of siRNA (Figure 5C; lanes 2 & 7). This was much more prominent from the flow cytometric analysis of γH2AX as a marker for DNA breakage at stalled forks, in which even a small amount of siRPA70 was sufficient to sensitize 5-Ph-IAA and ATRi-exposed cells to generate a new $\gamma H2AX^+$ peak that represents the excessive manifestation of fork collapse (Supplementary Figure S4D). Conversely, overexpression of three RPA subunits in a stoichiometric manner reduced the induction of replication damage signals including γH2AX and pKAP1 (Supplementary Figure S4E). These results indicate that the synergistic fork instability is attributed to inordinate ssDNA accumulation, rendering cells highly vulnerable to available RPA levels for preventing replication catastrophe.

We then wished to elucidate how ATR suppresses ssDNA accumulation in a synergistic manner at both local and global levels. First, acute TIM degradation was sufficient for triggering ATR activation and downstream CHK1 phosphorylation, which was mainly dependent on TOPBP1, an ATR activator at the ssDNA-dsDNA junction of stalled forks, rather than on ETAA1, which activates ATR via its interaction with stretches of RPA-coated ssDNA (Figure 5D, lanes 2, 4 & 6 and Supplementary Figure S5A). Indeed, TOPBP1 knockdown phenocopied ATR inhibition in sensitizing cells to 5-Ph-IAA (Figure 5D, lanes 5 & 6, pRPA32 and pKAP1), while co-depletion of ETAA1 and TOPBP1 caused a similar amount of excessive replication damage even in the absence of 5-Ph-IAA (Figure 5D, lanes 7 & 8), highlighting the role of ATR activation in counteracting replication damage elicited by replisome dysfunction.

Next, we determined if ATR stabilizes stalled forks by controlling local replisome activity. Replication pausing is an important function of the FPC in maintaining a stable replication complex at various fork barriers and under replication stress (33). While combination of 5-Ph-IAA and aphidicolin, an inhibitor of DNA polymerases that uncouples the helicase and polymerase activities, induced minimal ssDNA exposure, additional ATR inhibition triggered replication catastrophe, suggesting that ATR restricts replisome uncoupling (Figure 5E and Supplementary Figure S5B). In yeast, phosphorylation-defective Mrc1 (CLASPIN) mutant phenocopies the Rad53 (CHK1) mutant in its inability to counteract fork uncoupling, a phenotype negated by the deletion of Mrc1 itself, and Mrc1 phosphorylation by Rad53 slows down replication fork elongation *in vitro*, indicating that replication-promoting function of CLASPIN needs to be constrained by ATR-CHK1 at stalled forks to limit ssDNA exposure (34,41). Notably, knocking down CLASPIN partially suppressed the ssDNA accumulation elevated by the 5-Ph-IAA and ATRi combination, indicating that the ATR activity is necessary for attenuating the fork progression driven by CLASPIN in the FPC when TIM is acutely depleted and thus the CMG is unrestricted (Figure 5F and Supplementary Figure S5C).

We wanted to confirm this result using a different approach. A previous study demonstrated that polymerase α (PolA) inhibition causes extensive uncoupling of leading- and lagging-strands, ultimately leading to lethal RPA

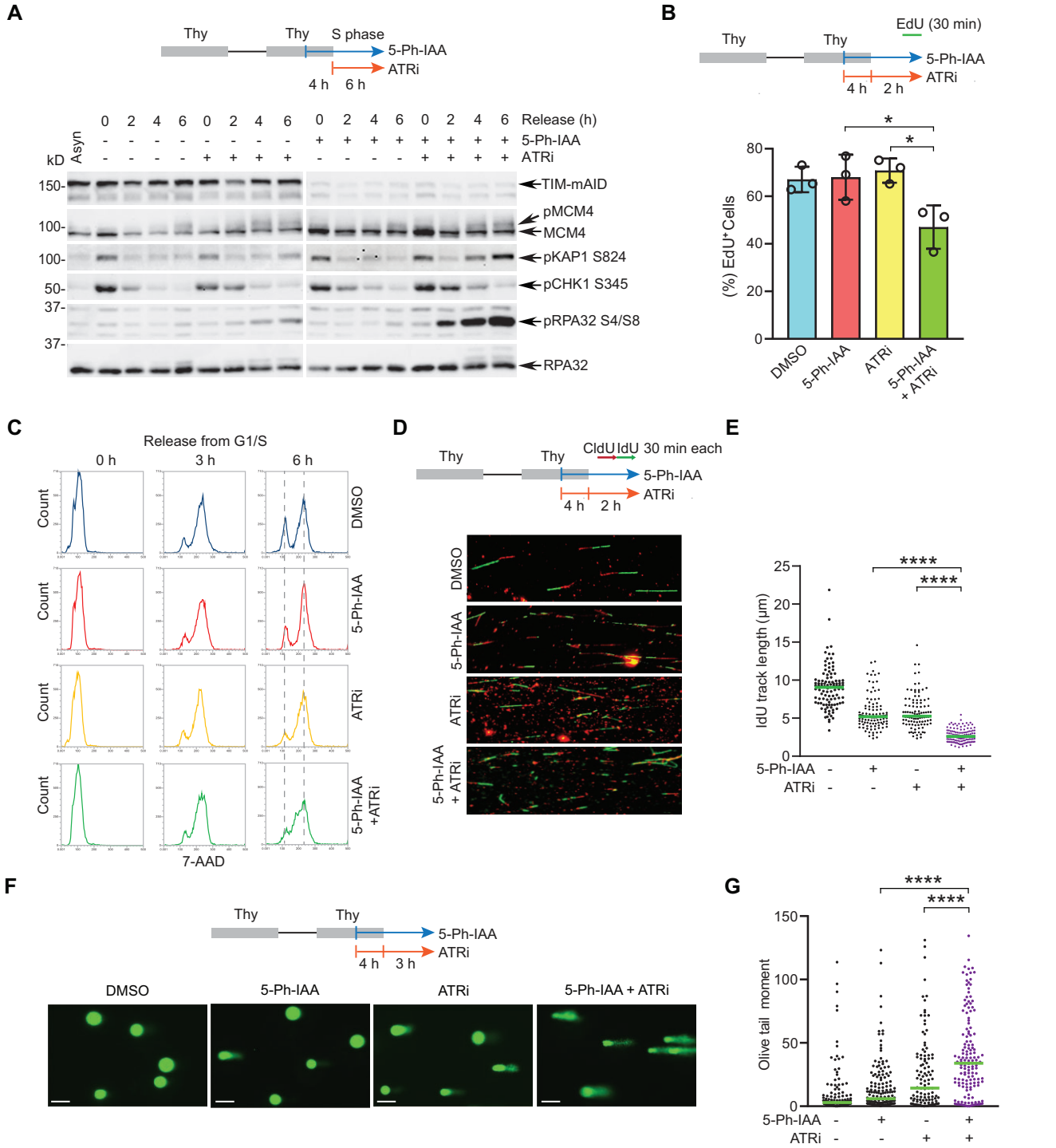

Figure 4. Acute TIM degradation and ATR inhibition results in fork progression defect and replication fork collapse. (**A**) TIM-mAID cells were synchronized by double thymidine block, depleted of TIM-mAID by 1 μM 5-Ph-IAA, and released into S phase in the presence of 1 μM ATRi. (**B**) Flow cytometric analysis of EdU incorporation in cells synchronized in G1/S boundary, depleted of TIM by 5-Ph-IAA, and released into S phase in the presence or absence of ATRi. 10 μM EdU was treated for 30 min prior to harvest during S phase progression. $n = 3$, mean ± SD, $^{*}P < 0.05$, Student's t-test. (**C**) Flow cytometry showing S phase progression from G1/S boundary in the presence of 5-Ph-IAA and/or ATRi. (**D**) Representative DNA fiber images from TIM-mAID cells synchronized at G1/S, treated with 5-Ph-IAA and/or ATRi as indicated, and replication forks dual-labeled to monitor fork progression. Scale bar: 5 μm. (**E**) Dot plot and median of the IdU track length. $n = 2$, >200 tracks per condition, $^{****}P < 0.0001$, Mann–Whitney test. (**F**) Representative images of DNA comets from TIM-mAID cells synchronized at G1/S, treated with 5-Ph-IAA and/or ATRi as indicated. Scale bar: 100 μm. (**G**) Quantification of DNA comet Olive tail moment. Green bars represent the median. $n = 2$, >100 nuclei per sample, $^{****}P < 0.0001$, Mann–Whitney test.

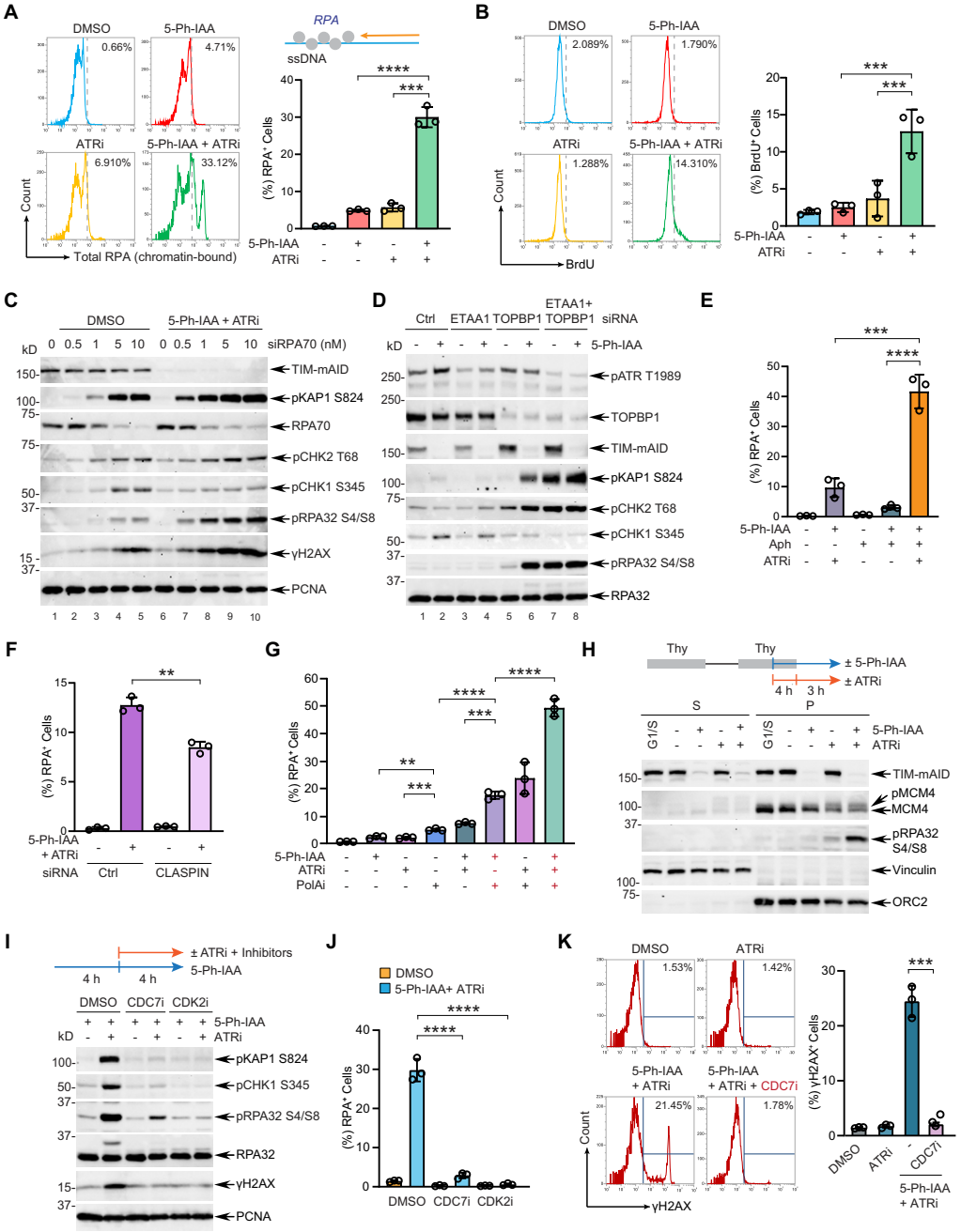

Figure 5. Both local and global roles of ATR counteract replication fork instability upon acute TIM degradation. (**A**) *Left*: histogram plot of chromatin-bound RPA32 in TIM-mAID cells treated with 1 μM 5-Ph-IAA and/or 1 μM ATRi for 8 h, and analyzed by flow cytometry. A vertical line defines background signal, and (%) RPA32-positive cells are denoted. *Right*: quantification, $n = 3$, mean ± SD, $^{***}P < 0.001$, Student's *t*-test. (**B**) *Left*: histogram plot of BrdU-positive cells in TIM-mAID cells, nascent DNA labeled by BrdU for 24 h, followed by 5-Ph-IAA and/or ATRi for 8 h, and analyzed by flow cytometry in a non-denaturing condition. *Right*: quantification, $n = 3$, mean ± SD, $^{***}P < 0.001$, Student's *t*-test. (**C**) TIM-mAID cells were transfected with siRNA RPA70 at the indicated dosage, cotreated with 5-Ph-IAA and ATRi for 8 h, and analyzed by WB. (**D**) TIM-mAID cells were transfected with indicated siRNAs for 72 h, treated with 5-Ph-IAA for 8 h, and analyzed by WB. (**E**) Quantification of RPA32-positive cells in TIM-mAID cells pretreated with 1 μM aphidicolin (Aph) for 1 h, followed by 5-Ph-IAA and/or ATRi for 5 h, and analyzed by flow cytometry. $n = 3$, mean ± SD, $^{****}P < 0.0001$, $^{***}P < 0.001$, Student's *t*-test. (**F**) Quantification of chromatin-bound RPA32 in TIM-mAID cells, transfected with siRNA CLASPIN (versus control), cotreated with 5-Ph-IAA and ATRi for 8 h. $n = 3$, mean ± SD, $^{***}P < 0.001$, Student's *t*-test. (**G**) Quantification of RPA32-positive cells in TIM-mAID cells pretreated with 1 μM (PolAi; ST1926) for 30 min, followed by followed by 5-Ph-IAA and/or ATRi for 5 h and analyzed by flow cytometry. $n = 3$, mean ± SD, $^{****}P < 0.0001$, $^{***}P < 0.001$, $^{**}P < 0.01$, Student's *t*-test. (**H**) TIM-mAID cells were synchronized by double thymidine block and treated with 5-Ph-IAA and/or and ATRi as indicated, cells were isolated into cytosolic/nucleoplasmic (S) versus chromatin-enriched (P) fractions, and MCM4 phosphorylation was analyzed by WB. An increased ratio of pMCM4 versus MCM4 indicates MCM4 hyper-phosphorylation. (**I**) TIM-mAID cells were treated with 5-Ph-IAA and/or ATRi together with 5 μM CDC7i (PHA-767491) or 5 μM CDK2i (SNS-032), and analyzed by WB. (**J**) Quantification of RPA32-positive cells in TIM-mAID cells treated with 5-Ph-IAA and/or ATRi together with CDC7i or CDK2i by flow cytometry. $n = 3$, mean ± SD, $^{****}P < 0.0001$, Student's *t*-test. (**K**) *Left*: histogram plot of γH2AX in TIM-mAID cells treated with 5-Ph-IAA, ATRi, and/or CDC7i for 8 h. *Right*: quantification, $n = 3$, mean ± SD, $^{***}P < 0.001$, Student's *t*-test.

exhaustion (40). Consistent with this, while PolAi itself caused accumulation of more ssDNA than 5-Ph-IAA or ATRi alone, 5-Ph-IAA administration on top of PolAi significantly exacerbated ssDNA accumulation at much higher levels than co-treatment of 5-Ph-IAA and ATRi, and combination of all three dramatically elevated ssDNA levels (Figure 5G). This further underscores the short-term effect of acute TIM depletion, which sensitizes ongoing replication forks to expose ssDNA while forks are still able to progress, and the ATR activity is required to restrict fork movement and thus prevent RPA exhaustion. Additionally, the proximity ligation signal between MCM6 and EdU-labeled replication forks, a readout of polymerase-helicase coupling, was significantly decreased by ATRi on top of 5-Ph-IAA treatment, indicating that ATR is necessary for replisome coupling in the absence of TIM (Supplementary Figure S5D). Together, these data suggest that ATR checkpoint signaling promotes pausing and stabilization of the replication machinery to limit ssDNA exposure when coordination within the replisome is disrupted upon rapid TIM degradation. This effect is in contrast to a long-term depletion of TIM by siRNA, which would severely impair fork progression by overall disruption of the FPC and replisome integrity.

At the same time, ATR inhibition results in hyperphosphorylation of MCM4 compared to control or 5-Ph-IAA only during S phase progression, indicating that dormant origin firing is unleashed (Figure 5H). Accordingly, inhibition of global dormant origin firing by a CDC7 inhibitor (PHA-767491) or a CDK2 inhibitor (SNS-032) was sufficient for abrogating pKAP1, pRPA32 and γH2AX that were elevated in cells exposed to 5-Ph-IAA and ATRi (Figure 5I). A suppressive role of CDC7 inhibition by PHA-767491 was also observed by the flow cytometric analysis of RPA32 accumulation and γH2AX induction (Figure 5J, K, and Supplementary Figure S5E). Another CDC7 inhibitor, TAK-931, was able to inhibit the synergistic fork instability at a comparable level (Supplementary Figure S5F, G). Notably, the amount of unleashed new origins was comparably increased in cells treated with ATRi only or in combination with 5-Ph-IAA, suggesting that dormant origin firing itself cannot fully explain the observed synergistic fork instability, which further underscores the role of ATR in integrating both local and global fork stabilization mechanisms (Supplementary Figure S5H). All together, these results suggest that both unrestricted CMG activity upon loss of TIM and unleashing of dormant origin firing in the absence of ATR activity synergistically triggers excessive ssDNA accumulation and RPA exhaustion, leasing to replication catastrophe.

Aberrant processing of stalled forks under the control of DNA-PK and CHK1 is responsible for the replication catastrophe of cells exposed to 5-ph-IAA and ATRi

We further wished to identify elements responsible for the manifestation of synergistic fork instability from acute TIM degradation and ATR inhibition. A stalled fork frequently undergoes fork reversal, a process involving regression of the stalled fork to form a four-way junction, in which the nascent-strand ssDNA is subject to nucleolytic degradation if not properly protected (42). Multiple structure-specific nucleases as well as endo/exonucleases are known to control the processing of fork cleavage and DNA end resection. For instance, ATR phosphorylates SMARCAL1, a fork reversal translocase, to restrict fork regression activities and prevent aberrant fork processing (6). Indeed, immunoblots revealed that depletion of SMARCAL1 reduces the elevated pRPA32 and pKAP1 levels in cells exposed to 5-Ph-IAA and ATRi (Figure 6A). We also observed that individual knockdown of SLX4, a scaffold of the SLX4-SLX1 Holliday junction resolvase and a coordinator of XPF and MUS81 nucleases, MUS81 itself, or CtIP, a 5′-flap endonuclease necessary for the resection of breaks, resulted in a decrease of stalled fork instability. Similar inhibitory results were observed in the flow cytometric analysis of γH2AX to measure DSB formation (Figure 6B and Supplementary Figure S6A). Additionally, treatment with mirin, an inhibitor of MRE11 which is an exonuclease responsible for the processing of reversed forks, was sufficient to abrogate the $\gamma H2AX^{+}$ cells against 5-Ph-IAA and ATRi (Figure 6C). Together, these results suggest that acute TIM loss and ATR inhibition leads to increased reversal of stalled forks, which becomes a substrate of aberrant fork processing, leading to DSB formation and fork collapse.

To identify the signaling that controls the fork processing and collapse in cells exposed to 5-Ph-IAA and ATRi, we turned our attention to CHK1 activation in the absence of ATR activity most prominent at later time points (Figure 3A–D). DNA-PK, another ATR and ATM-related phosphatidylinositol 3-kinase-related kinase (PIKK) family member, is known to phosphorylate CHK1 to promote fork recovery in ATRi-treated cells (8). Intriguingly, prolonged treatment of 5-Ph-IAA and ATRi led to the activation of DNA-PK, which was associated with pCHK1 induction (Figure 6D). Pharmacological inhibition of DNA-PK was sufficient for abolishing CHK1 phosphorylation as well as its known phosphorylation target, pRPA32 S4/S8, while CHK1 inhibition itself amplified pCHK1 S345 in an ATR-dependent manner as previously reported (43) (Figure 6E). Importantly, either DNA-PK or CHK1 inhibition suppressed the induction of pKAP1 and pRPA32 and reduced γH2AX levels (Figure 6E, F, and Supplementary Figure S6B). On the other hand, ATM inhibition failed to suppress elevated γH2AX levels. Also, brief incubation of CHK1i after induction of DNA-PK activation (i.e. 6 h post 5-Ph-IAA and ATRi) was sufficient to suppress γH2AX (Supplementary Figure S6C). Application of DNA-PKi and CHK1i together further suppressed γH2AX in comparison to the single treatments, indicating that DNK-PK may have other targets besides CHK1 for the propagation of signaling that culminates in replication catastrophe (Supplementary Figure S6D). Remarkably, while CHK1i caused γH2AX induction to a similar level to ATRi when combined with 5-Ph-IAA, combination of 5-Ph-IAA, ATRi, and CHK1i together alleviated the replication catastrophe caused by 5-Ph-IAA and ATRi treatment, suggesting that CHK1 inhibition is antagonistic to ATRi in this context (Figure 6G). DNA-PK inhibition itself did not cause any major toxicity in combination with others (Supplementary Figure S6E). Accordingly, short-term CHK1 inhibition rescued the cellular viability of cells exposed to 5-Ph-IAA and

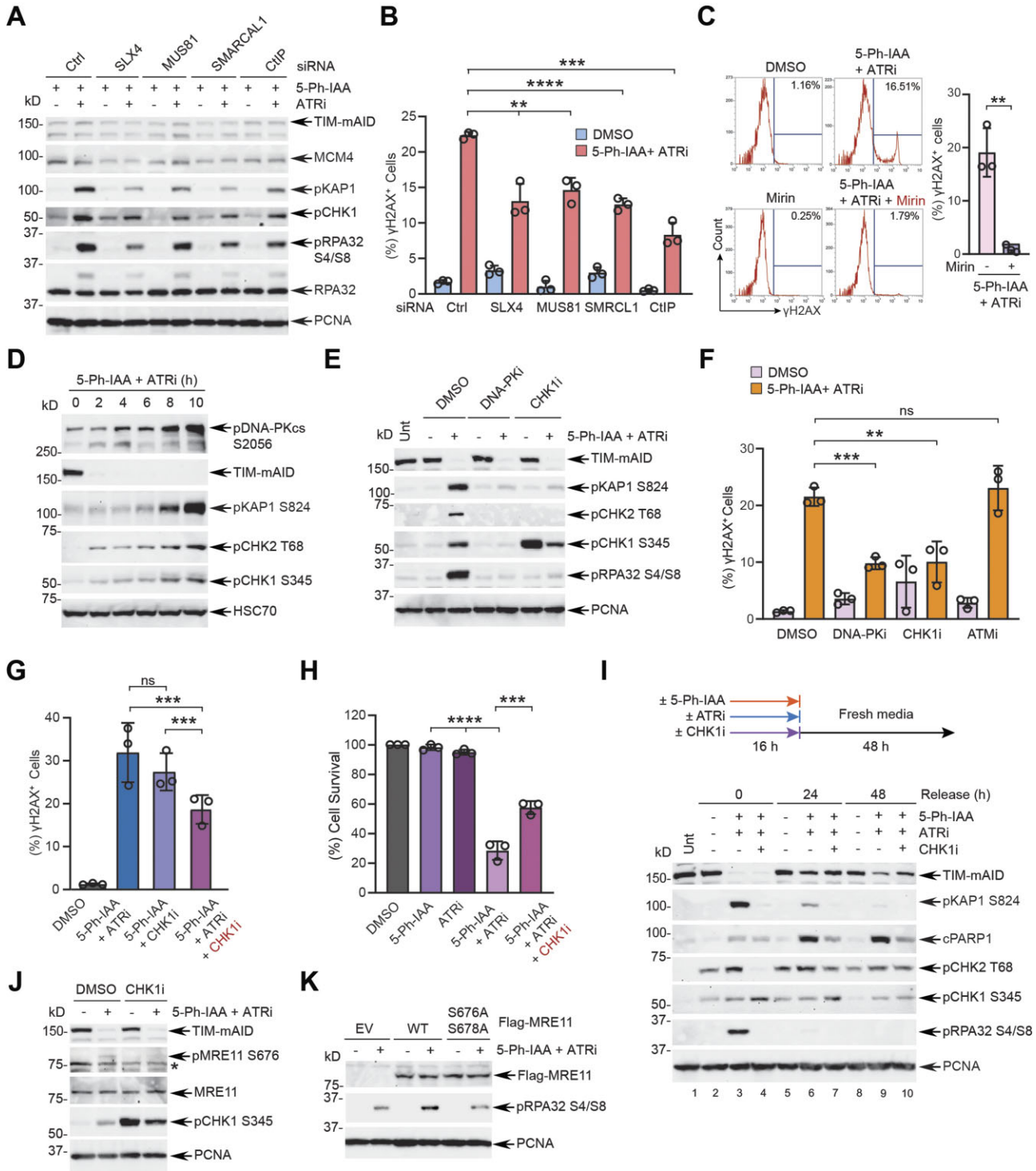

Figure 6. Aberrant enzymatic processing of reversed forks controlled by the DNA-PK-CHK1 axis is responsible for the replication catastrophe. (**A**) TIM-mAID cells were transfected with indicated siRNAs for 72 h, treated with 1 μM 5-Ph-IAA and/or 1 μM ATRi for 8 h, and analyzed by WB. (**B**) Quantification of γH2AX-positive cells transfected with indicated siRNAs and treated with 5-Ph-IAA and/or ATRi, analyzed by flow cytometry. $n = 3$, mean ± SD, $^{****}P < 0.0001$, $^{***}P < 0.001$, $^{**}P < 0.01$, Student's *t*-test. (**C**) *Left*: histogram plot of γH2AX in TIM-mAID cells treated with 5-Ph-IAA and ATRi together with 1 μM mirin for 8 h. *Right*: quantification, $n = 3$, $^{**}P < 0.01$, Student's *t*-test. (**D**) TIM-mAID cells treated with 5-Ph-IAA and ATRi were harvested at the indicated times and CHK1 activation was analyzed by WB. (**E**) TIM-mAID cells were treated with 5-Ph-IAA and ATRi together with 5 μM DNA-PKi (NU7441) or 5 μM CHK1i (MK8776) and analyzed by WB. (**F, G**) Quantification of γH2AX-positive cells treated with 5-Ph-IAA, ATRi, and 5 μM DNA-PKi (NU7441), 5 μM CHK1i, or 10 μM ATMi (KU55933) in combination, analyzed by flow cytometry. $n = 3$, mean ± SD, $^{***}P < 0.001$, $^{**}P < 0.01$, n.s. not significant, Student's *t*-test. (**H**) Cytotoxicity of TIM-mAID cells measured by ATP-dependent luminescence. $n = 3$, mean ± SD, $^{****}P < 0.0001$, $^{***}P < 0.001$, Student's *t*-test. (**I**) TIM-mAID cells treated with 5-Ph-IAA/ATRi and/or CHKi for were released into fresh media for 24 or 48 h, and cell death was evaluated by cPARP1 WB. (**J**) WB analysis of pMRE11 S676 in TIM-mAID cells treated with 5-Ph-IAA/ATRi for 8 h. *: non-specific bands. (**K**) pRAP32 S4/S8 WB analysis of cells transfected with Flag-MRE11 wild-type or S676A/S678A and treated with 5-Ph-IAA and ATRi.

ATRi and recovered to fresh media, measured by cellular ATP and PARP1 cleavage as well as γH2AX accumulation (Figure 6H, I; lanes 6 & 7, 9 & 10, and Supplementary Figure S6F). Interestingly, CHK1 inhibition largely failed to suppress ssDNA accumulation, indicating that CHK1 works downstream of exposed ssDNA but upstream of DSB formation (Supplementary Figure S6G, H). Together, these results suggest that a DNA-PK-CHK1 axis is engaged at stalled forks in response to ATR and TIM deficiency to promote replication catastrophe, which is separable from the initial role of CHK1 under the canonical ATR-CHK1 checkpoint to counteract the replication damage triggered by acute TIM loss. In this sense, CHK1 plays a dual role, i.e. fork protection and fork destabilization, depending on the status of ATR at TIM-deficient stalled forks.

Lastly, we determined the specific role of the DNA-PK-CHK1 axis toward replication fork instability. DNA replication stress and DSBs are known to trigger the phosphorylation of MRE11 at S676 and S678, which is necessary for controlling DNA resection and stalled fork processing via homology-directed repair (44,45). Intriguingly, we observed that combined 5-Ph-IAA and ATRi triggers MRE11 phosphorylation at S676, revealed by a phospho-specific antibody, which is abrogated by CHK1 inhibition (Figure 6J and Supplementary Figure S6I). Additionally, ectopic expression of MRE11 wild-type, but not the phospho-dead mutant, augmented pRPA32 S4/S8 induction triggered by 5-Ph-IAA and ATRi, supporting the role of MRE11 phosphorylation in promoting replication catastrophe (Figure 6K). Together, these results suggest that the DNA-PK-CHK1 signaling cascade controls MRE11 activity to promote synergistic fork instability and replication catastrophe under the condition of TIM loss and ATR inactivation.

DISCUSSION

Using auxin-inducible TIM degradation as a model to elicit endogenous replication stress, we elucidated the ATR-dependent local and global checkpoint mechanisms in counteracting replication catastrophe against acute replisome dysfunction (Figure 7). In otherwise unperturbed conditions, rapid TIM loss at ongoing forks causes transient replisome uncoupling and triggers activation of the ATR-CHK1 checkpoint, which on one hand, stabilizes the unrestricted replisome at TIM-deficient stalled forks, and on the other hand, suppresses dormant origin firing to limit ssDNA accumulation. Conversely, ATR inhibition upon acute TIM depletion synergistically exposes ssDNA sufficient for exhausting available RPA pools, due to excessive replisome uncoupling and origin firing, ultimately leading to irreversible fork collapse and replication catastrophe. The synergistic fork instability is only observed with the combination of TIM degradation and ATR inhibition, suggesting that ATR connects its local role in replisome stabilization to its global role of CDK control. While this integrated model extends the earlier study describing an indispensable reliance on ATR upon TIM knockdown and reinforces the RPA exhaustion model whereby fork breakage associated with extensively exposed ssDNA is a common denominator of massive fork collapse (14,46), it provides additional insight that the TIM-deficient replisome at stalled forks needs to be restrained by the ATR-CHK1 checkpoint to prevent the uncoupling of both helicase-polymerase activities and leading/lagging-strand synthesis. Degrading TIM or treating HU does not generate extensive ssDNA at an early phase unless active ATR is disabled (Supplementary Figure S4B and Figure 5A), and HU-induced fork collapse occurs rather later after insults, presumably when new origin firing has gradually accumulated (47), indicating that there exists a specific mechanism to constrain the replisome progression and exposure of ssDNA at stalled forks. Conversely, replisome stabilization is not necessarily the main and sole function of the ATR checkpoint in preventing fork collapse, suggesting that both local and global branches of checkpoint surveillance need to operate simultaneously (48,49). ATR-CHK1 is indispensable for preventing fork breakage at unchallenged forks and replicating fragile sites (50–52). Our TIM-mAID model reflects the physiological infliction of endogenous replication stress, such as stochastic replisome dysfunction, progression through difficult-to-replicate regions and DNA repeats, and oncogene activation during which replication forks could be challenged, thereby underscoring the coordinated efforts between the FPC and ATR to guard the replicating genome in a collective way.

How the ATR-CHK1 checkpoint modifies the replisome to limit the replisome uncoupling remains unclear. One mechanism would be to attenuate the replication function of the FPC, allowing it to work as a pausing complex at stalled forks. While stimulating polymerase activities, TIM inhibits the helicase activity of the CMG *in vitro* (53). In budding yeast, asymmetric leading- and lagging-strand synthesis and ssDNA formation manifested in *Rad53*-deficient or *Mrc1* phospho-dead mutants is suppressed by the loss of Tof1 or Mrc1, indicating that the replication checkpoint restrains the CMG in order to prevent excessive replisome uncoupling at stalled forks (34). Indeed, Rad53 phosphorylates Mrc1 to slow down fork elongation *in vitro* (41). CLASPIN is able to accelerate leading-strand progression *in vitro* without TIM (25); accordingly, we showed that CLASPIN depletion antagonizes replisome uncoupling and ssDNA exposure caused by TIM and ATR deficiency. Given the localization of TIM ahead of the CMG and its role in replisome pausing, we envision that rapid TIM loss sensitizes stalled forks to CLASPIN-mediated fork progression, and unrestricted CMG function driven by CLASPIN at TIM-deficient forks contributes to ssDNA exposure unless the ATR-CHK1 checkpoint constrains its activity. Pharmacological uncoupling of leading- and lagging-strands by a Polα inhibitor is sufficient for lethal ssDNA accumulation and replication catastrophe, underscoring that the CMG-polymerase function needs to be restricted upon fork stalling (40). Displacement of TIM from the replisome under oxidative stress conditions to slow fork progression has been reported (54). Also, CHK1 is necessary for slowing down fork elongation following replication damage (19). Hence, direct modification of the FPC or associated replisome components may regulate how a fork progresses or pauses, which will dictate how much ssDNA would be generated at stalled forks. For instance, ATR phosphorylates and recruits FANCD2 to the fork via its interaction with MCMs, which slows polymerase progression and restricts resection of stalled forks (55).

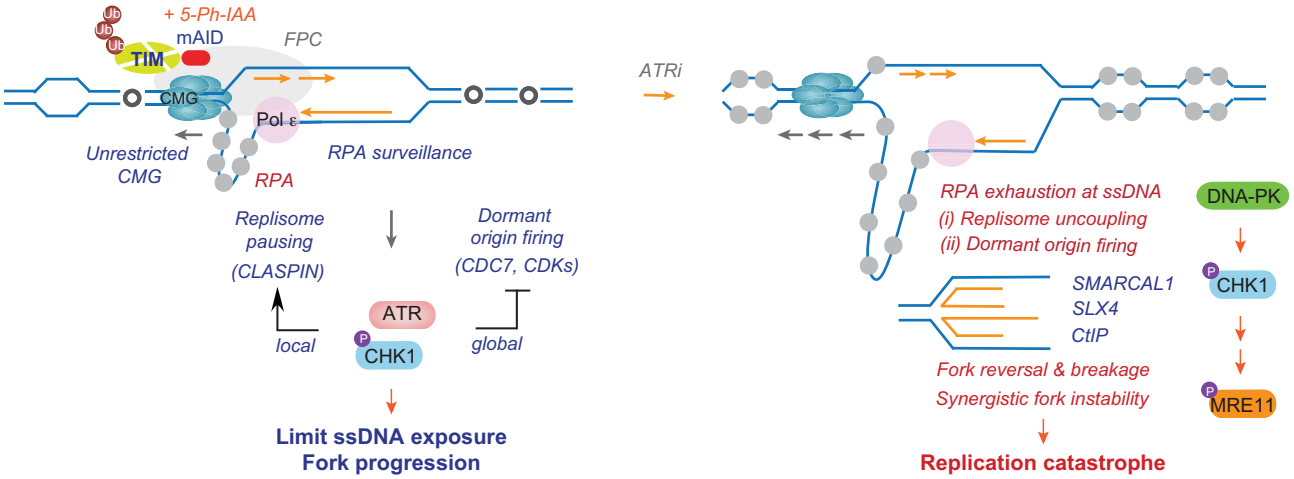

Figure 7. Model for the mechanism of synergistic fork instability at the TIM-deficient stalled fork. The basal-level ATR activity monitors RPA levels and ssDNA exposure during DNA replication. Acute degradation of TIM results in unrestricted CMG activity, sensitizing a replication fork to replisome uncoupling and ssDNA exposure, while the fork is still competent to progress. This triggers the ATR-CHK1 checkpoint, which integrates fork stabilization mechanisms operating both at the local level to stabilize the replication complex by constraining fork progression (e.g. modification of CLASPIN) and at the global level to suppress dormant origin firing. Replisome coupling and minimal ssDNA exposure ensures fork stability and fork progression against acute replisome dysfunction. Accordingly, ATR inhibition leads to synergistic fork instability by massive ssDNA accumulation, leading to RPA exhaustion and replication catastrophe. Aberrant nucleolytic processing of a reversed fork, mediated by the DNA-PK-CHK1 signaling cascade (e.g. MRE11 phosphorylation), contributes to irreversible fork collapse and cell death.

Our study also supports that massive fork collapse stemming from TIM degradation and ATR inactivation is an active process driven by multiple structure-specific nucleases and endo/exonucleases. While the replication checkpoint is necessary for preventing nuclease-mediated replication fork cleavage, whether it directly regulates nuclease activities is unclear (56). Extensive fork collapse may result from deregulated fork processing such as fork reversal, which may dictate the point in which RPA is exhausted. Phosphorylation of SMARCAL1 by ATR is known to suppress fork reversal *in vitro* and fork collapse in cells (6). Indeed, we showed that SMARCAL1 depletion decreases the level of DSBs associated with replication catastrophe. We also observed that SLX4, in part, contributes to the formation of DSBs upon TIM depletion and ATR inhibition, which is in line with a previous report in ATR-inhibited cells (6). Furthermore, conversion of stalled forks to DSBs is dependent on MUS81 under replication damage or checkpoint inhibition, which may be necessary for fork restart through homologous recombination or alternative recombination pathways (57,58). Together, our data and others suggest that aberrant fork remodeling and processing in the excess of ssDNA and in the absence of checkpoint regulation leads to irreversible fork collapse. The synergistic fork instability may in part result from high CDK activity upon checkpoint inhibition. For instance, CDK upregulation by WEE1 kinase inhibition is associated with SLX4 phosphorylation and recruitment of MUS81 (59). MRE11 supports MUS81-dependent fork processing in checkpoint-deficient cells (60,61), and we also identified that MRE11 is responsible for the replication catastrophe caused by TIM loss and ATR inhibition, further illuminating how multiples nuclease activities integrate to aberrantly process stalled forks and cause fork collapse when replication stress is over the threshold.

Intriguingly, the DNA-PK-CHK1 axis turned out to relay the replication stress signaling, culminating in replication catastrophe. A similar DNA-PK-CHK1 pathway arising from ATR inhibition was noted, which works as a backup mechanism to suppress origin firing and counteract replication stress (8). However, in our case, CHK1 inhibition suppresses DSB formation and the cytotoxicity of TIM loss and ATR inhibition, indicating that there is a distinct CHK1-driven mechanism, controlled by DNA-PK independently of the canonical ATR-CHK1 checkpoint, which contributes to the processing of ssDNA-exposed stalled forks, subsequently fork collapse and cell death. MRE11 phosphorylation is under the control of DNA-PK-CHK1, suggesting that the DNA-PK-CHK1 signaling cascade controls the nucleolytic processing of stalled forks, leading to fork collapse. DNA-PK localizes at replication forks and forms complexes with RPA *in vitro* and in cells (62,63). DNA-PK may become activated when it is repositioned from the RPA-ssDNA complex to DSBs progressively accumulating at stalled forks in the absence of ATR. Under the synergistic fork instability when TIM is lost and ATR is inhibited, it may recognize CHK1 as a new substrate besides its canonical substrate RPA32 for the phosphorylation at S4/S8, although detailed mechanisms need to be elucidated.

In summary, our study defines a physiological fork surveillance mechanism mediated by ATR that integrates both local and global checkpoints to monitor the replisome integrity and limit ssDNA exposure at replication forks. This basal ATR activity becomes essential upon acute TIM degradation, which essentially mimics the condition of replisome uncoupling and uncoordinated replication. Given the high expression of TIM in a variety of cancer and an increased tolerance to oncogene-induced replication stress by TIM (64), we anticipate that targeting the

architecture or function of the FPC may provide a way to exploit the replication vulnerability of cancer cells with elevated replication stress and to augment the efficacy of ATR inhibitors.

DATA AVAILABILITY

All data is available in the main text and supplemental materials. Plasmids and cell lines generated for this study will be made available upon request.

SUPPLEMENTARY DATA

Supplementary Data are available at NAR Online.

ACKNOWLEDGEMENTS

We would like to thank Dr M. Kanemaki (National Institute of Genetics, Japan) for providing the HCT116 OsTIR1 F74G cell line and 5-Ph-IAA, and Dr Claudia Lukas (U. Copenhagen, DK) for the pAcGFP-C1-RPA123-P2A construct. We thank the members in the Kim laboratory for helpful discussions and comments in the manuscript.
Author contributions: J.A.P. established the HCT116 TIM-mAID cell line and performed most of the experiments with help from C.Z., J.R., J.S. and A.K. H.K. conceptualized and supervised the project, and wrote the manuscript with the assistance of J.A.P.

FUNDING

National Institutes of Health [R01GM144399]; American Cancer Society [RSG-18-037-DMC]; Breast Cancer Alliance (to H.K.); American Cancer Society Institutional Research Grant (to J.R.). Funding for open access charge: National Institutes of Health [R01GM144399].
Conflict of interest statement. None declared.

REFERENCES

1. Branzei,D. and Foiani,M. (2010) Maintaining genome stability at the replication fork. *Nat. Rev. Mol. Cell Biol.*, **11**, 208–219.
2. Zeman,M.K. and Cimprich,K.A. (2014) Causes and consequences of replication stress. *Nat. Cell Biol.*, **16**, 2–9.
3. Cong,K. and Cantor,S.B. (2022) Exploiting replication gaps for cancer therapy. *Mol. Cell*, **82**, 2363–2369.
4. Cimprich,K.A. and Cortez,D. (2008) ATR: an essential regulator of genome integrity. *Nat. Rev. Mol. Cell Biol.*, **9**, 616–627.
5. Saldivar,J.C., Cortez,D. and Cimprich,K.A. (2017) The essential kinase ATR: ensuring faithful duplication of a challenging genome. *Nat. Rev. Mol. Cell Biol.*, **18**, 622–636.
6. Couch,F.B., Bansbach,C.E., Driscoll,R., Luzwick,J.W., Glick,G.G., Betous,R., Carroll,C.M., Jung,S.Y., Qin,J., Cimprich,K.A. *et al.* (2013) ATR phosphorylates SMARCAL1 to prevent replication fork collapse. *Genes Dev.*, **27**, 1610–1623.
7. Davies,S.L., North,P.S. and Hickson,I.D. (2007) Role for BLM in replication-fork restart and suppression of origin firing after replicative stress. *Nat. Struct. Mol. Biol.*, **14**, 677–679.
8. Buisson,R., Boisvert,J.L., Benes,C.H. and Zou,L. (2015) Distinct but concerted roles of ATR, DNA-PK, and Chk1 in countering replication stress during S phase. *Mol. Cell*, **59**, 1011–1024.
9. Saldivar,J.C., Hamperl,S., Bocek,M.J., Chung,M., Bass,T.E., Cisneros-Soberanis,F., Samejima,K., Xie,L., Paulson,J.R., Earnshaw,W.C. *et al.* (2018) An intrinsic S/G2 checkpoint enforced by ATR. *Science*, **361**, 806–810.
10. Santocanale,C. and Diffley,J.F. (1998) A Mec1- and Rad53-dependent checkpoint controls late-firing origins of DNA replication. *Nature*, **395**, 615–618.
11. Ge,X.Q. and Blow,J.J. (2010) Chk1 inhibits replication factory activation but allows dormant origin firing in existing factories. *J. Cell Biol.*, **191**, 1285–1297.
12. Yin,Y., Lee,W.T.C., Gupta,D., Xue,H., Tonzi,P., Borowiec,J.A., Huang,T.T., Modesti,M. and Rothenberg,E. (2021) A basal-level activity of ATR links replication fork surveillance and stress response. *Mol. Cell*, **81**, 4243–4257.
13. Toledo,L.I., Altmeyer,M., Rask,M.B., Lukas,C., Larsen,D.H., Povlsen,L.K., Bekker-Jensen,S., Mailand,N., Bartek,J. and Lukas,J. (2013) ATR prohibits replication catastrophe by preventing global exhaustion of RPA. *Cell*, **155**, 1088–1103.
14. Toledo,L., Neelsen,K.J. and Lukas,J. (2017) Replication catastrophe: when a checkpoint fails because of exhaustion. *Mol. Cell*, **66**, 735–749.
15. Chen,Y.H., Jones,M.J., Yin,Y., Crist,S.B., Colnaghi,L., Sims,R.J., Rothenberg,E., Jallepalli,P.V. and Huang,T.T. (2015) ATR-mediated phosphorylation of FANCI regulates dormant origin firing in response to replication stress. *Mol. Cell*, **58**, 323–338.
16. Moiseeva,T., Hood,B., Schamus,S., O'Connor,M.J., Conrads,T.P. and Bakkenist,C.J. (2017) ATR kinase inhibition induces unscheduled origin firing through a Cdc7-dependent association between GINS and And-1. *Nat. Commun.*, **8**, 1392.
17. Moiseeva,T.N., Yin,Y., Calderon,M.J., Qian,C., Schamus-Haynes,S., Sugitani,N., Osmanbeyoglu,H.U., Rothenberg,E., Watkins,S.C. and Bakkenist,C.J. (2019) An ATR and CHK1 kinase signaling mechanism that limits origin firing during unperturbed DNA replication. *Proc. Natl. Acad. Sci. U.S.A.*, **116**, 13374–13383.
18. Mailand,N., Falck,J., Lukas,C., Syljuasen,R.G., Welcker,M., Bartek,J. and Lukas,J. (2000) Rapid destruction of human Cdc25A in response to DNA damage. *Science*, **288**, 1425–1429.
19. Petermann,E., Woodcock,M. and Helleday,T. (2010) Chk1 promotes replication fork progression by controlling replication initiation. *Proc. Natl. Acad. Sci. U.S.A.*, **107**, 16090–16095.
20. Leman,A.R. and Noguchi,E. (2012) Local and global functions of timeless and Tipin in replication fork protection. *Cell Cycle*, **11**, 3945–3955.
21. Jo,U., Cai,W., Wang,J., Kwon,Y., D'Andrea,A.D. and Kim,H. (2016) PCNA-dependent cleavage and degradation of SDE2 regulates response to replication stress. *PLos Genet.*, **12**, e1006465.
22. Rageul,J., Park,J.J., Jo,U., Weinheimer,A.S., Vu,T.T.M. and Kim,H. (2019) Conditional degradation of SDE2 by the Arg/N-End rule pathway regulates stress response at replication forks. *Nucleic Acids Res.*, **47**, 3996–4010.
23. Rageul,J., Park,J.J., Zeng,P.P., Lee,E.A., Yang,J., Hwang,S., Lo,N., Weinheimer,A.S., Scharer,O.D., Yeo,J.E. *et al.* (2020) SDE2 integrates into the TIMELESS-TIPIN complex to protect stalled replication forks. *Nat. Commun.*, **11**, 5495.
24. Weinheimer,A.S., Paung,Y., Rageul,J., Khan,A., Lo,N., Ho,B., Tong,M., Alphonse,S., Seeliger,M.A. and Kim,H. (2022) Extended DNA binding interfaces beyond the canonical SAP domain contribute to the function of replication stress regulator SDE2 at DNA replication forks. *J. Biol. Chem.*, **298**, 102268.
25. Baris,Y., Taylor,M.R.G., Aria,V. and Yeeles,J.T.P. (2022) Fast and efficient DNA replication with purified human proteins. *Nature*, **606**, 204–210.
26. Yeeles,J.T.P., Janska,A., Early,A. and Diffley,J.F.X. (2017) How the eukaryotic replisome achieves rapid and efficient DNA replication. *Mol. Cell*, **65**, 105–116.
27. Baretic,D., Jenkyn-Bedford,M., Aria,V., Cannone,G., Skehel,M. and Yeeles,J.T.P. (2020) Cryo-EM structure of the fork protection complex bound to CMG at a replication fork. *Mol. Cell*, **78**, 926–940.
28. Jones,M.L., Baris,Y., Taylor,M.R.G. and Yeeles,J.T.P. (2021) Structure of a human replisome shows the organisation and interactions of a DNA replication machine. *EMBO J.*, **40**, e108819.
29. Kemp,M.G., Akan,Z., Yilmaz,S., Grillo,M., Smith-Roe,S.L., Kang,T.H., Cordeiro-Stone,M., Kaufmann,W.K., Abraham,R.T., Sancar,A. *et al.* (2010) Tipin-replication protein A interaction mediates Chk1 phosphorylation by ATR in response to genotoxic stress. *J. Biol. Chem.*, **285**, 16562–16571.
30. Unsal-Kacmaz,K., Chastain,P.D., Qu,P.P., Minoo,P., Cordeiro-Stone,M., Sancar,A. and Kaufmann,W.K. (2007) The

human Tim/Tipin complex coordinates an Intra-S checkpoint response to UV that slows replication fork displacement. *Mol. Cell. Biol.*, **27**, 3131–3142.
31. Yoshizawa-Sugata,N. and Masai,H. (2007) Human Tim/Timeless-interacting protein, Tipin, is required for efficient progression of S phase and DNA replication checkpoint. *J. Biol. Chem.*, **282**, 2729–2740.
32. Patel,J.A. and Kim,H. (2023) The TIMELESS effort for timely DNA replication and protection. *Cell. Mol. Life Sci.*, **80**, 84.
33. Katou,Y., Kanoh,Y., Bando,M., Noguchi,H., Tanaka,H., Ashikari,T., Sugimoto,K. and Shirahige,K. (2003) S-phase checkpoint proteins Tof1 and Mrc1 form a stable replication-pausing complex. *Nature*, **424**, 1078–1083.
34. Serra-Cardona,A., Yu,C., Zhang,X., Hua,X., Yao,Y., Zhou,J., Gan,H. and Zhang,Z. (2021) A mechanism for Rad53 to couple leading- and lagging-strand DNA synthesis under replication stress in budding yeast. *Proc. Natl. Acad. Sci. U.S.A.*, **118**, e2109334118.
35. Nishimura,K., Fukagawa,T., Takisawa,H., Kakimoto,T. and Kanemaki,M. (2009) An auxin-based degron system for the rapid depletion of proteins in nonplant cells. *Nat. Methods*, **6**, 917–922.
36. Yesbolatova,A., Saito,Y., Kitamoto,N., Makino-Itou,H., Ajima,R., Nakano,R., Nakaoka,H., Fukui,K., Gamo,K., Tominari,Y. *et al.* (2020) The auxin-inducible degron 2 technology provides sharp degradation control in yeast, mammalian cells, and mice. *Nat. Commun.*, **11**, 5701.
37. Foote,K.M., Nissink,J.W.M., McGuire,T., Turner,P., Guichard,S., Yates,J.W.T., Lau,A., Blades,K., Heathcote,D., Odedra,R. *et al.* (2018) Discovery and characterization of AZD6738, a potent inhibitor of ataxia telangiectasia mutated and Rad3 related (ATR) kinase with application as an anticancer agent. *J. Med. Chem.*, **61**, 9889–9907.
38. Moeglin,E., Desplancq,D., Conic,S., Oulad-Abdelghani,M., Stoessel,A., Chiper,M., Vigneron,M., Didier,P., Tora,L. and Weiss,E. (2019) Uniform widespread nuclear phosphorylation of histone H2AX is an indicator of lethal DNA replication stress. *Cancers (Basel)*, **11**, 355.
39. Forment,J.V. and Jackson,S.P. (2015) A flow cytometry-based method to simplify the analysis and quantification of protein association to chromatin in mammalian cells. *Nat. Protoc.*, **10**, 1297–1307.
40. Ercilla,A., Benada,J., Amitash,S., Zonderland,G., Baldi,G., Somyajit,K., Ochs,F., Costanzo,V., Lukas,J. and Toledo,L. (2020) Physiological tolerance to ssDNA enables strand uncoupling during DNA replication. *Cell Rep.*, **30**, 2416–2429.
41. McClure,A.W. and Diffley,J.F. (2021) Rad53 checkpoint kinase regulation of DNA replication fork rate via Mrc1 phosphorylation. *Elife*, **10**, e69726.
42. Neelsen,K.J. and Lopes,M. (2015) Replication fork reversal in eukaryotes: from dead end to dynamic response. *Nat. Rev. Mol. Cell Biol.*, **16**, 207–220.
43. Morgan,M.A., Parsels,L.A., Zhao,L., Parsels,J.D., Davis,M.A., Hassan,M.C., Arumugarajah,S., Hylander-Gans,L., Morosini,D., Simeone,D.M. *et al.* (2010) Mechanism of radiosensitization by the Chk1/2 inhibitor AZD7762 involves abrogation of the G2 checkpoint and inhibition of homologous recombinational DNA repair. *Cancer Res.*, **70**, 4972–4981.
44. Kijas,A.W., Lim,Y.C., Bolderson,E., Cerosaletti,K., Gatei,M., Jakob,B., Tobias,F., Taucher-Scholz,G., Gueven,N., Oakley,G. *et al.* (2015) ATM-dependent phosphorylation of MRE11 controls extent of resection during homology directed repair by signalling through Exonuclease 1. *Nucleic Acids Res.*, **43**, 8352–8367.
45. Somyajit,K., Spies,J., Coscia,F., Kirik,U., Rask,M.B., Lee,J.H., Neelsen,K.J., Mund,A., Jensen,L.J., Paull,T.T. *et al.* (2021) Homology-directed repair protects the replicating genome from metabolic assaults. *Dev. Cell*, **56**, 461–477.
46. Smith,K.D., Fu,M.A. and Brown,E.J. (2009) Tim-Tipin dysfunction creates an indispensible reliance on the ATR-Chk1 pathway for continued DNA synthesis. *J. Cell Biol.*, **187**, 15–23.
47. Petermann,E., Orta,M.L., Issaeva,N., Schultz,N. and Helleday,T. (2010) Hydroxyurea-stalled replication forks become progressively inactivated and require two different RAD51-mediated pathways for restart and repair. *Mol. Cell*, **37**, 492–502.
48. Dungrawala,H., Rose,K.L., Bhat,K.P., Mohni,K.N., Glick,G.G., Couch,F.B. and Cortez,D. (2015) The replication checkpoint prevents two types of fork collapse without regulating replisome stability. *Mol. Cell*, **59**, 998–1010.
49. De Piccoli,G., Katou,Y., Itoh,T., Nakato,R., Shirahige,K. and Labib,K. (2012) Replisome stability at defective DNA replication forks is independent of S phase checkpoint kinases. *Mol. Cell*, **45**, 696–704.
50. Casper,A.M., Nghiem,P., Arlt,M.F. and Glover,T.W. (2002) ATR regulates fragile site stability. *Cell*, **111**, 779–789.
51. Sorensen,C.S. and Syljuasen,R.G. (2012) Safeguarding genome integrity: the checkpoint kinases ATR, CHK1 and WEE1 restrain CDK activity during normal DNA replication. *Nucleic Acids Res.*, **40**, 477–486.
52. Syljuasen,R.G., Sorensen,C.S., Hansen,L.T., Fugger,K., Lundin,C., Johansson,F., Helleday,T., Sehested,M., Lukas,J. and Bartek,J. (2005) Inhibition of human Chk1 causes increased initiation of DNA replication, phosphorylation of ATR targets, and DNA breakage. *Mol. Cell. Biol.*, **25**, 3553–3562.
53. Cho,W.H., Kang,Y.H., An,Y.Y., Tappin,I., Hurwitz,J. and Lee,J.K. (2013) Human Tim-Tipin complex affects the biochemical properties of the replicative DNA helicase and DNA polymerases. *Proc. Natl. Acad. Sci. U.S.A.*, **110**, 2523–2527.
54. Somyajit,K., Gupta,R., Sedlackova,H., Neelsen,K.J., Ochs,F., Rask,M.B., Choudhary,C. and Lukas,J. (2017) Redox-sensitive alteration of replisome architecture safeguards genome integrity. *Science*, **358**, 797–802.
55. Lossaint,G., Larroque,M., Ribeyre,C., Bec,N., Larroque,C., Decaillet,C., Gari,K. and Constantinou,A. (2013) FANCD2 binds MCM proteins and controls replisome function upon activation of s phase checkpoint signaling. *Mol. Cell*, **51**, 678–690.
56. Lopes,M., Cotta-Ramusino,C., Pellicioli,A., Liberi,G., Plevani,P., Muzi-Falconi,M., Newlon,C.S. and Foiani,M. (2001) The DNA replication checkpoint response stabilizes stalled replication forks. *Nature*, **412**, 557–561.
57. Forment,J.V., Blasius,M., Guerini,I. and Jackson,S.P. (2011) Structure-specific DNA endonuclease Mus81/Eme1 generates DNA damage caused by Chk1 inactivation. *PLoS One*, **6**, e23517.
58. Dehe,P.M. and Gaillard,P.H.L. (2017) Control of structure-specific endonucleases to maintain genome stability. *Nat. Rev. Mol. Cell Biol.*, **18**, 315–330.
59. Duda,H., Arter,M., Gloggnitzer,J., Teloni,F., Wild,P., Blanco,M.G., Altmeyer,M. and Matos,J. (2016) A mechanism for controlled breakage of under-replicated chromosomes during mitosis. *Dev. Cell*, **39**, 740–755.
60. Techer,H., Koundrioukoff,S., Carignon,S., Wilhelm,T., Millot,G.A., Lopez,B.S., Brison,O. and Debatisse,M. (2016) Signaling from Mus81-Eme2-dependent DNA damage elicited by Chk1 deficiency modulates replication fork speed and origin usage. *Cell Rep.*, **14**, 1114–1127.
61. Thompson,R., Montano,R. and Eastman,A. (2012) The Mre11 nuclease is critical for the sensitivity of cells to Chk1 inhibition. *PLoS One*, **7**, e44021.
62. Shao,R.G., Cao,C.X., Zhang,H., Kohn,K.W., Wold,M.S. and Pommier,Y. (1999) Replication-mediated DNA damage by camptothecin induces phosphorylation of RPA by DNA-dependent protein kinase and dissociates RPA:DNA-PK complexes. *EMBO J.*, **18**, 1397–1406.
63. Dibitetto,D., Marshall,S., Sanchi,A., Liptay,M., Badar,J., Lopes,M., Rottenberg,S. and Smolka,M.B. (2022) DNA-PKcs promotes fork reversal and chemoresistance. *Mol. Cell*, **82**, 3932–3942.
64. Bianco,J.N., Bergoglio,V., Lin,Y.L., Pillaire,M.J., Schmitz,A.L., Gilhodes,J., Lusque,A., Mazieres,J., Lacroix-Triki,M., Roumeliotis,T.I. *et al.* (2019) Overexpression of Claspin and Timeless protects cancer cells from replication stress in a checkpoint-independent manner. *Nat. Commun.*, **10**, 910.